

1 **An Unusual Case of Rapid Cyclogenesis in the northeast Pacific Basin.**

2 **Part I: Overview and Piecewise PV Inversion.**

3 Patrick T. Beaty,^a Jonathan E. Martin,^a Andrew C. Winters,^b Gary M. Lackmann^c

4 ^a *University of Wisconsin-Madison*

5 ^b *University of Colorado-Boulder*

6 ^c *North Carolina State University*

7

8

9

10

11

12

13

14

15

16

17

18

19

20

21

22

23

24

25 Corresponding author: Patrick T. Beaty, pbeaty@wisc.edu

26
27
28
29
30
31
32
33
34
35
36
37
38
39
40
41
42
43
44
45
46
47
48
49
50

ABSTRACT

A case of extremely rapid extratropical cyclogenesis over the northeast Pacific Ocean in late November 2019 is examined. The development is of particular interest as much of the strengthening occurred in an unusual environment characterized by cold sea surface temperatures. Cyclogenesis began as a weak but stationary upstream surface low in the north-central Pacific ushered warm, moist tropical air poleward towards a pre-existing surface frontal boundary, resulting in intense lower-tropospheric frontogenesis. The resulting thermally direct vertical circulation mobilized a diabatic Rossby wave (DRW) which moved eastward along the baroclinic zone. An intensifying upper-level jet/front system draping equatorward from Alaska became favorably aligned with the low-level DRW on its approach towards the California-Oregon border to force deepening rates as high as 6 hPa hr^{-1} prior to landfall.

Analysis of this storm provides an opportunity to interrogate explosive DRW development over a cold sea surface. The 3D Ertel potential vorticity (PV) structure associated with this storm is partitioned into separate upper-tropospheric, lower-tropospheric, and diabatically-induced anomalies which are separately inverted to recover the flow associated with each piece. Analysis of this partitioned PV reveals that development followed a bottom-up sequence by which near-surface PV dominated early cyclogenesis, diabatically-induced PV dominated a large period of subsequent intensification, and upper-tropospheric PV dominated the final period of development. It is shown that diabatic influences in response to vigorous latent heat release are responsible for much of the lower-tropospheric cyclogenesis with an upper-level jet/front system becoming an important driver for the rapid cyclogenesis observed immediately before landfall.

51

SIGNIFICANCE STATEMENT

52 A rapidly-developing low-pressure system over the northeast Pacific Ocean in late
53 November 2019 set all-time low pressure records and occurred in an unusual region of
54 the world. The analysis shows that this development occurred from the bottom-up and
55 mid-tropospheric latent heat release was the most important process leading to its record
56 strength. It is very uncommon for low-pressure systems of this intensity to follow a
57 bottom-up development. More work is needed to determine how the upper- and lower-
58 tropospheric features interacted with each other as they conspired to produce this record-
59 setting low-pressure system.

60 **1. Introduction**

61 Rapid extratropical cyclogenesis, colloquially known as "bomb" cyclogenesis (e.g.,
62 Sanders and Gyakum 1980; Roebber 1984) arises from a variety of different dynamical and
63 thermodynamical factors including the interaction between upper-level troughs and lower-
64 level baroclinic zones (e.g., Sanders 1986; Gyakum et al. 1992; Lagouvardos et al. 2007; Heo
65 et al. 2019), diabatic heating in the form of latent heat release, (e.g., Bosart 1981; Roebber
66 1993; Martin and Otkin 2004) and/or sea-surface heat fluxes (e.g., Davis and Emanuel 1988;
67 Roebber 1989; Kuo et al. 1991; Gyakum and Danielson 2000; Kouroutzoglou et al. 2015). In
68 addition, the interaction between a diabatic Rossby wave (DRW) and an upper-level trough
69 (e.g., Wernli et al. 2002; Moore et al. 2008; Rivière et al. 2010; Boettcher and Wernli 2011,
70 2013; McKenzie 2014; Zhang and Wang 2018) is a particular kind of rapid cyclogenesis
71 event. The concept of a DRW was introduced in a series of studies in the early 1990s (i.e.,
72 Raymond and Jiang 1990; Snyder and Lindzen 1991; Parker and Thorpe 1995). All three of
73 these studies employed highly idealized models with cloud-diabatic feedbacks in the vicinity
74 of lower-troposphere baroclinic zones to consider both the production, and subsequent
75 evolution, of positive low-level potential vorticity (PV) anomalies beneath the location of
76 maximum cloud production.

77 Studies by Moore and Montgomery (2004, 2005) were the first to classify such low-level
78 PV anomalies as diabatically-generated vortices. The synergy between the associated cyclonic
79 flow around such a vortex and the baroclinic zone along which it forms acts to provide
80 continued positive moisture and temperature advections downstream of the vortex. These
81 advections contribute to the production of clouds and precipitation, which serve to generate or
82 extend the lower-tropospheric cyclonic PV anomaly downstream, thereby appearing to
83 propagate the original anomaly downstream.

84 In late December 1999, winter storm *Lothar* devastated portions of western Europe,
85 becoming the costliest windstorm in European history in terms of structural and ecological
86 damage (Wernli et al. 2002). Focusing their analysis of the event on the evolution of a DRW,
87 Wernli et al. (2002) showed that *Lothar* underwent a ‘bottom-up’ development in which the
88 low-level cyclonic PV anomaly (the DRW), acting on an initially zonal upper-level flow,
89 induced upper-level trough development which eventually enabled a superposition of upper-
90 and lower-level PV features. Though bottom-up development of explosive DRWs with no
91 pre-existing upper-level trough is rare (Boettcher and Wernli 2013), such a configuration
92 served to initiate the mutual amplification of the two features which was manifest in the rapid
93 development of *Lothar*. Rivière et al. (2010) employed the Météo-France operational model
94 to perform a sensitivity analysis of the development of *Lothar* and, though analysis was
95 centered around the investigation of *Lothar*, the conclusions were extended to explosive
96 development of DRWs in general. They found that the explosive growth stage of rapidly
97 developing DRWs such as *Lothar* are highly dependent on 1) moist processes to overcome
98 frictional and turbulent dissipation, 2) the location of the upper-level jet exit region to aid in
99 synoptic-scale ascent, and 3) a lower-level baroclinic zone to encourage DRW self-
100 sustenance.

101 Boettcher and Wernli (2011) used four European Centre for Medium-Range Weather
102 Forecasts (ECMWF) model forecasts initialized at different lead times along with a DRW-
103 tracking algorithm to interrogate the influence of downstream lower-tropospheric temperature
104 and moisture advections on rapid DRW developments. Boettcher and Wernli (2013)
105 constructed a 10-year climatology of DRWs in the Northern Hemisphere based on the
106 tracking algorithm developed in Boettcher and Wernli (2011). These consecutive studies led
107 to the identification of four precursor environments favorable for DRW genesis: 1) a broad
108 subtropical high advecting warm air and moisture towards a baroclinic zone, 2) a cutoff low
109 or remnant tropical cyclone advecting warm air and moisture towards a baroclinic zone, 3) an

110 upper-level trough moving over a lower-tropospheric baroclinic zone, and 4) the remnants of
111 a tropical cyclone or mesoscale convective system propagating along a baroclinic zone as a
112 lower-level vortex. Frequent locations of rapid DRW developments in the Northern
113 Hemisphere were along the Gulf Stream in the Atlantic Ocean and following the
114 climatological North Pacific wintertime jet (Boettcher and Wernli 2013). In addition, they
115 suggested that most cases of explosive DRW development involve a DRW interacting with a
116 pre-existing upper-level trough.

117 Moore et al. (2008) and Rivière et al. (2010) both took advantage of the utility of the
118 piecewise PV inversion method introduced by Davis and Emanuel (1991) to attribute the
119 intensification of a DRW cyclogenesis event to discrete pieces of the full column PV. The
120 cases chosen for both studies were DRWs propagating over warm sea surface temperatures
121 (SSTs) which provides substantial surface heat and moisture fluxes to aid in the rapid
122 strengthening of the DRW (e.g., Davis and Emanuel 1988; Roebber 1989; Kuo et al. 1991;
123 Gyakum and Danielson 2000; Kouroutzoglou et al. 2015). To the best of the authors'
124 knowledge, a similar analysis on an explosive DRW development over cold SSTs has not yet
125 been performed.

126 Over a 24-hour period from 0000 UTC 26 November to 0000 UTC 27 November
127 2019, a diabatic Rossby wave (DRW) originating at the intersection of a high θ_e tropical
128 moisture plume and a zonally oriented baroclinic zone underwent rapid cyclogenesis over the
129 northeast Pacific Ocean. DRW intensification followed the description offered by Boettcher
130 and Wernli (2013), wherein low-level diabatically-generated PV associated with the DRW
131 vortex became vertically collocated with an upper-level PV anomaly borne of a downward
132 and equatorward surge of stratospheric air. This superposition of forcings resulted in a
133 maximum central mean sea level pressure (MSLP) fall of 49 hPa in 24 hours as the DRW
134 progressed east-southeastward towards the United States West Coast. As the storm neared
135 landfall, the MSLP dropped 12 hPa between 1600 UTC and 1900 UTC 26 November,

136 including a 1-hour central MSLP fall of 6 hPa from 1700 UTC to 1800 UTC 26 November
137 2019. The observed MSLP of 973.4 hPa at Crescent City, California at 0300 UTC 27
138 November 2019 set the all-time low sea-level pressure record for the state of California.
139 November low sea-level pressure records were also observed in Medford, Oregon (981.4 hPa)
140 and Eureka, California (984.4 hPa) on the same date.

141 The November 2019 cyclone provides an opportunity to interrogate the nature of an
142 explosive DRW development over a cold ocean current. The analysis will center on a
143 piecewise PV inversion of this particular cyclone following the method of Davis and Emanuel
144 (1991). Comparing this event to those previously examined (over warm SSTs) will highlight
145 physical precursors critical for rapid DRW-induced development in such an otherwise
146 unfavorable environment. The paper is organized as follows. Section 2 provides a synoptic
147 evolution of the lifecycle of the November 2019 cyclone from 12 hours before genesis to
148 post-occlusion and affirms that this is a DRW-induced development while highlighting its
149 exceptional nature. An overview of the reanalysis data and the piecewise PV inversion
150 method utilized in this study is detailed in section 3. The evolution of the lifecycle of the
151 storm through the lens of piecewise PV inversion is discussed in section 4. Comparison of
152 this event to the bottom-up development of *Lothar* along with conclusions and suggestions for
153 further analysis are offered in section 5.

154 **2. Synoptic Evolution and Anomalous Nature**

155 *a. Overview*

156 We use hourly data from the ECMWF reanalysis version 5 (ERA5; Hersbach et al. 2020)
157 to describe the synoptic overview of the November 2019 (hereafter NV19) storm and will
158 focus on twelve hour increments from 1200 UTC 25 November 2019, prior to the nascent
159 stage of development, to 1200 UTC 27 November 2019, past the period of its most rapid

160 development and nine hours after the storm made landfall on the West Coast of the United
161 States.

162 1) 1200 UTC 25 November 2019

163 Twelve hours before the NV19 storm developed its own closed circulation at sea-level, a
164 predominantly zonally-oriented surface baroclinic zone, indicated by a strong gradient of 950
165 hPa equivalent potential temperature (θ_e) contours, was draped southeastward from an almost
166 cutoff low pressure system to the west through the center of a strong surface anticyclone to
167 the east (Fig. 1a). Though there was no closed isobar evident at this time, there was a 950 hPa
168 relative vorticity maximum (yellow-highlighted “X”) at the intersection of this baroclinic
169 zone with a more meridionally oriented cold frontal baroclinic zone (Figs. 1a,b). The same
170 baroclinic zones were reflected in the isentropes at 850 hPa, with positive frontogenesis
171 occurring due east of the 950 hPa vorticity maximum and a separate region extending towards
172 the cutoff low pressure system to the southwest (Fig. 1c). The strongest positive frontogenesis
173 was along the warm front near and east of the surface development region. Positive
174 frontogenesis was maximized between 850 and 900 hPa along the baroclinic zone on which
175 the cyclone developed, with negative omega (ascent) focused on the warm side of a deep
176 baroclinic zone in response to that frontogenesis (Fig. 1d). At 500 hPa, the surface
177 development region was downstream of the nearly cutoff low pressure center to the southwest
178 and a shortwave feature to the northwest over the Alaska Peninsula (Fig. 1e). A region of
179 cyclonic vorticity advection (CVA) by the thermal wind, indicative of column mass
180 divergence and ascent (Sutcliffe 1947), was located west of the development region (not
181 shown). The surface development region was also centered in the right entrance region of a
182 downstream, anticyclonically-curved jet streak at 300 hPa characterized by weak along-flow
183 acceleration in the entrance region (Fig. 1f). The upper-level shortwave as represented in the

184 300 hPa PV field was situated over the Aleutian Islands as was the shortwave at 500 hPa
185 (Figs. 1e,f).

186 2) 0000 UTC 26 November 2019

187 By 0000 UTC 26 November 2019, a weak surface cyclone was discernable along the
188 baroclinic zone that stretched zonally through the anticyclone (Fig. 2a). This disturbance had
189 begun to develop its own separate cloud feature by this time (Fig. 2b). The 850 hPa baroclinic
190 zone and positive frontogenesis maintained its previous spatial relationship with the
191 developing surface cyclone (Fig. 2c), with frontogenesis located to the east and northeast of
192 the surface cyclone along the developing warm front. Positive frontogenesis was now
193 maximized at 800 hPa as the frontal slope notably steepened from the previous time (compare
194 Fig. 1d to Fig. 2d). In response to this evolution, the tropospheric ascent associated with the
195 lower-tropospheric frontogenesis was deeper. The shortwave feature at 500 hPa began to
196 strengthen to the northwest of the surface cyclone, indicated by the increase in positive
197 relative vorticity along the shortwave axis (Fig. 2e). The presence of this shortwave resulted
198 in a region of CVA by the thermal wind more proximate to the surface cyclone at this time.
199 At 300 hPa, the surface cyclone maintained its position relative to the right entrance region of
200 the downstream, anticyclonically-curved jet streak with now stronger along-flow speed
201 change characterizing the entrance region (Fig. 2f). The shortwave feature at 300 hPa had also
202 strengthened as indicated by the expanding region of large 300 hPa positive PV to the north-
203 northwest of the surface cyclone.

204 3) 1200 UTC 26 November 2019

205 Twelve hours after initial development, the NV19 storm had completely bisected the
206 anticyclone within which it initially developed (Fig. 3a). Well-defined cold and warm fronts
207 now characterized the cyclone, as shown by the 950 hPa θ_e , with pressure troughs associated
208 with both fronts. At this time, the storm was beginning its twelve-hour period of most rapid

209 deepening as it approached the California-Oregon border. The storm was also beginning to
210 transition from a baroclinic leaf (R. B. Weldon 1979) to a more classic comma shape (Fig.
211 3b). The primary band of positive frontogenesis at 850 hPa remained robust and associated
212 with the surface warm front while a band of weaker, positive frontogenesis developed along
213 the cold front (Fig. 3c). The cyclone center was now clearly located at the apex of the 850 hPa
214 thermal ridge. Positive frontogenesis peaked at 700 hPa as the warm front neared its
215 maximum strength, while the frontal slope continued to steepen (Figs. 2d, 3d). Ascent
216 expanded and intensified throughout the depth of the mid- to lower-troposphere, now being
217 maximized around 750 hPa. Rapid intensification and elongation of the 500 hPa positive
218 vorticity feature occurred to the west-northwest of the surface cyclone, coincident with a
219 sharp temperature gradient, indicative of the development of a potent upper-level jet/front
220 system (Fig. 3e). This intensification focused vigorous CVA by the thermal wind directly
221 above the surface cyclone and, consequently, the central pressure of the NV19 storm began to
222 rapidly drop. The thermal trough indicated by the 1000-500 hPa thickness also lagged the
223 geopotential height trough with a thermal ridge slightly downstream of it. The thermal
224 gradient directly west of the cyclone had intensified within this same twelve-hour interval.
225 The region of increased baroclinicity was reflected in an increase in wind speed at 300 hPa, at
226 the base of the shortwave feature (Fig. 3f). This wind speed intensification also situated the
227 NV19 storm in the left exit region of a newly formed jet streak tied to the development of the
228 upper-level jet/front system (e.g. Shapiro 1981, 1983; Lackmann et al. 1997; Martin 2014),
229 providing another mechanism for enhancing upper-level mass evacuation and lower-
230 tropospheric cyclogenesis.

231 4) 0000 UTC 27 November 2019

232 In the twenty-four hours after initial development, the storm had deepened a total of 47
233 hPa to a central MSLP of 971 hPa, well exceeding the definition of explosive cyclogenesis

234 first defined in Sanders and Gyakum (1980) (Fig. 4a). In fact, the storm had deepened from
235 1020 hPa at 2200 UTC 25 November to 971 hPa at 2200 UTC 26 November, resulting in a
236 maximum 24-hour deepening rate of 49 hPa. At 0000 UTC 27 November, the NV19 storm
237 was just a few hours from making landfall on the west coast of the United States near
238 Crescent City, California (Figs. 4a,b). The intense pressure gradient to the south of the
239 cyclone center resulted in surface winds greater than 45 m s^{-1} near the California-Oregon
240 border and 23 m waves off the California coast. By this time, the positive frontogenesis at 850
241 hPa associated with the warm front was undoubtedly influenced by the steep topography
242 adjacent to the United States West Coast (Fig. 4c) as the frontal structure had clearly
243 weakened (Fig. 4d). Lower-tropospheric ascent at this time reached its largest values of the
244 cyclone lifecycle. A well-developed trough with substantial CVA by the thermal wind and an
245 elongated streamer of vorticity at 500 hPa were both still forcing ascent in and around the
246 surface cyclone (Fig. 4e), with the strongest CVA by the thermal wind situated south of the
247 cyclone (not shown). The intensified vortex strip was a manifestation of the continued
248 development of the associated upper-level jet/front system (Fig. 4e). The jet streak to the west
249 of the surface cyclone increased in intensity and the surface cyclone remained in the left exit
250 region as the jet raced southeastward on the upstream side of a newly carved out upper trough
251 (Fig. 4f). The surface cyclone was now vertically stacked as the 300 hPa PV and 500 hPa
252 vorticity were all maximized at the same location directly above the surface cyclone (Fig.
253 4e,f).

254 5) 1200 UTC 27 November 2019

255 Some nine hours after making landfall, the NV19 storm began to fill as it moved inland
256 (Figs. 5a,b). The 850 hPa frontogenesis was no longer active (Fig. 5c). In fact, the lack of
257 well-defined surface frontal regions is clearly indicated by the isentropes both in the
258 horizontal (at 850 hPa) and vertical directions (Figs. 5c,d). At 500 hPa, a circular geopotential

259 height minimum characterized by strong CVA on its southwestern edge was located directly
260 over the surface cyclone (Fig. 5e). The strong thermal contrast at this level, coincident with a
261 linear shear vorticity feature, was the final product of a robust upper-front development. The
262 left exit region of the jet streak and the 300 hPa PV feature were now located to the south of
263 the surface cyclone (Fig. 5f).

264 *b. The NV19 cyclone as a Diabatic Rossby wave*

265 As first introduced by Raymond and Jiang (1990), Snyder and Lindzen (1991), and
266 Parker and Thorpe (1995) and first classified by Moore and Montgomery (2004, 2005), a
267 DRW is a lower-tropospheric vortex borne of positive PV production in the vicinity of a
268 lower-tropospheric baroclinic zone that is situated below mid-tropospheric latent heat release.
269 During the early development phase of the NV19 storm, a nearly cutoff low pressure system
270 south of the Aleutian Islands and an expansive high pressure system off the coast of the
271 Pacific Northwest conspired to produce southerly flow which overan a predominantly zonal
272 baroclinic zone stretching across the northeast Pacific Ocean at 1200 UTC 25 November 2019
273 (Fig. 6a). This southerly flow induced strong lower-tropospheric frontogenesis which, in turn,
274 spawned the production of precipitation along the baroclinic zone as indicated by the 12-hour
275 rainfall rates from the ERA5 data. A lower-tropospheric circulation developed as a result of
276 the latent heat release that accompanied the production of precipitation. This circulation then
277 propagated along the baroclinic zone for at least the next 12 hours as shown by the location of
278 the SLP minimum along the mean 950 hPa θ_e gradient averaged between 1200 UTC 25
279 November and 0000 UTC 26 November 2019 (Fig. 6b). Thus, there was strong frontogenesis
280 and moist ascent along the baroclinic zone (Figs. 1c,d and 2c,d) driving precipitation
281 development and latent heat release which, in turn, mobilized lower-tropospheric diabatic PV
282 “production” (Fig. 6a,b). The resulting diabatically-generated vortex provided differential
283 temperature advection near the surface which then propagated the DRW vortex.

284 *c. The anomalous nature of the NV19 storm*

285 Northwesterly flow cyclogenesis events over the northeast Pacific Ocean are common
286 and well-documented (Reed and Albright 1986; Yoshiike and Kawamura 2009; Lang and
287 Martin 2012; Iwao et al. 2012; Iizuka et al. 2013) along with explosive cyclogenesis (EC)
288 events over this part of the Pacific Ocean (Roebber 1984; Wang and Rogers 2001; Boettcher
289 and Wernli 2013; Zhang et al. 2017). Despite the relative frequency of EC events over the
290 northeastern Pacific Ocean, the storm track, deepening rate, and location of maximum
291 deepening for the NV19 storm were all well outside of established climatologies for this part
292 of the world.

293 First, the NV19 storm had an unusual track. Roebber (1984) constructed a climatology of
294 Northern Hemisphere EC events over the period from 1976 to 1982 while Wang and Rogers
295 (2001) compiled a similar climatology for the period from 1985 to 1996. In still another
296 climatology (from 2000 to 2015), Zhang et al. (2017) specifically focused on EC events over
297 the northern Pacific Ocean. All three studies highlighted preferred regions for periodic EC
298 events: off the east coast of Japan, off the east coast of the United States, and in the central
299 Gulf of Alaska. After genesis, a majority of the cyclones track southwest to northeast based
300 on the roughly 30-year period covered by the three, non-consecutive climatologies. The
301 NV19 cyclone also initially formed in the central Gulf of Alaska and tracked nearly due east
302 before beginning a northwest to southeast track (Figs. 1-5). Zhang et al. (2017) divided their
303 database of EC storm tracks into separate regions of the northern Pacific in which clustering
304 of cyclogenesis events occurred. The storm track of the NV19 cyclone was approximately 90°
305 out of phase with the northeastern Pacific Ocean EC storm tracks from the climatology (their
306 Fig. 5e). The NV19 track was also mainly outside of the storm track densities presented in
307 Roebber (1984), Wang and Rogers (2001), and Zhang et al. (2017). It is clear that the storm
308 track associated with the NV19 storm was unusual based on at least 30 years of non-
309 consecutive climatologies presented in the literature.

310 Second, the deepening rate of EC events has been quantified using the "Bergeron" since it
311 was originally defined by Sanders and Gyakum (1980) as

312

313

$$1 \text{ Bergeron} = \frac{24 \text{ hPa}}{24 \text{ hours}} \cdot \frac{\sin(\phi)}{\sin(60^\circ)} \quad (1)$$

314 where ϕ is the latitude of the cyclone center normalized to 60°N. A cyclogenesis event must
315 accomplish a deepening rate equivalent to at least 1 Bergeron to be classified as explosive.
316 Roebber (1984) and Zhang et al. (2017) used normalized latitudes of 42.5° and 45°,
317 respectively, in the denominator of (1) as these mean latitudes were more representative of the
318 mean latitude of explosive cyclogenesis events presented in their studies. The deepening rate
319 of the NV19 storm using the Roebber (1984) and the Zhang et al. (2017) definitions was 2.14
320 Bergerons and 2.04 Bergerons, respectively. This deepening rate ranks the NV19 storm in the
321 99th percentile when focusing on the 115 EC cases over the northern Pacific Ocean from the
322 Roebber (1984) climatology and in the 93rd percentile when focusing on the 120 EC cases
323 over the northeast Pacific region from the Zhang et al. (2017) climatology. Further, the
324 maximum 6-hour deepening rate of 22 hPa between 1200 UTC to 1800 UTC 26 November
325 2019 rivals that of the maximum 6-hour deepening rate of 26 hPa accomplished by the *Braer*
326 storm, the strongest extratropical cyclone on record based both on minimum SLP and
327 deepening rate (Lim and Simmonds 2002; Odell et al. 2013). Therefore, the maximum 6-hour
328 deepening rate of the NV19 storm was among the strongest ever recorded for all extratropical
329 cyclones in the Pacific and Atlantic Ocean basins.

330 Finally, frequency contours of northern Pacific Ocean EC events are provided using
331 the Roebber (1984), Wang and Rogers (2001), and Zhang et al. (2017) climatologies (Fig. 7).
332 The furthest eastward extent of any of these frequency contours is 130°W (Fig. 7c). The

333 maximum deepening of the NV19 storm occurred between 1700 UTC and 1800 UTC 26
334 November 2019 to the east of 130°W longitude. Out of a combined 30-year period of
335 northern Pacific Ocean EC events, no other EC event has had a maximum deepening location
336 as far east as the NV19 storm, yet another aspect of its anomalous nature.

337 **3. Methods**

338 *a. Dataset*

339 Wind speed and direction, temperature, geopotential height, relative humidity, and
340 MSLP data for the NV19 storm were extracted on a limited area domain extending from 10°N
341 to 75°N and 180° to 90°W from the ERA5 data set. The analysis employs ERA5 data at 1-
342 hour intervals from 0000 UTC 01 November to 2300 UTC 31 December 2019 with a
343 horizontal grid spacing of $0.25^\circ \times 0.25^\circ$ and 19 vertical levels from 1000 hPa to 100 hPa at a
344 vertical grid spacing of 50 hPa. ERA5 data were then regridded to a grid spacing of $1.0^\circ \times$
345 1.0° as coarse data with smooth gradients is amenable for the PV inversion process (Hoskins
346 et al. 1985).

347 *b. Piecewise PV inversion*

348 One form of the Ertel PV (EPV) as first defined in Rossby (1940) and Ertel (1942) is
349 given as

$$EPV = -g (\zeta_\theta + f) \frac{\partial \theta}{\partial p} \quad (2)$$

350 where g is gravitational acceleration, ζ_θ is the isentropic relative vorticity, f is the planetary
351 vorticity, and $\frac{\partial \theta}{\partial p}$ is a static stability term. EPV is conserved for adiabatic, inviscid flow.
352 Information about the atmospheric flow associated with a distribution of EPV can be
353 extracted through the process of PV inversion (Hoskins et al. 1985; Davis and Emanuel

1991). The inversion of a distribution of PV requires knowledge of (1) a horizontal and vertical distribution of PV, (2) prescribed boundary conditions on the domain, and (3) a balance condition which relates the mass to the momentum field. It can be particularly enlightening to partition the PV field into discrete pieces each related to different vertical levels and/or physical processes involved in cyclogenesis, a technique known as *piecewise PV inversion* first introduced by Davis and Emanuel (1991, hereafter DE). Such piecewise PV inversion isolates the mass and momentum fields associated with individual pieces of the total anomalous PV, thus enabling investigation of the effect of each piece on the overall circulation tendency and the advection of the other pieces of the PV. The manner in which the PV is partitioned is thus crucially important to both the procurement and the precision of the resulting insights.

The DE inversion method assumes hydrostatic balance and that the magnitude of the rotational part of the flow is much larger than that of the divergent part of the flow. Applying these approximations to the divergence equation and equation (2) results in the system of equations, in spherical coordinates, used in the DE piecewise PV inversion:

$$\nabla^2 \Phi = \nabla \cdot (f \nabla \psi) + \frac{2}{a^4 \cos^2 \phi} \frac{\partial}{\partial (\lambda, \phi)} \left(\frac{\partial \psi}{\partial \lambda}, \frac{\partial \psi}{\partial \phi} \right) \quad (3)$$

$$\text{EPV} = \frac{g \kappa \pi}{p} \left[(f + \nabla^2 \psi) \frac{\partial^2 \Phi}{\partial^2 \pi} - \frac{1}{a^2 \cos^2 \phi} \frac{\partial^2 \psi}{\partial \lambda \partial \pi} \frac{\partial^2 \Phi}{\partial \lambda \partial \pi} - \frac{1}{a^2} \frac{\partial^2 \psi}{\partial \phi \partial \pi} \frac{\partial^2 \Phi}{\partial \phi \partial \pi} \right], \quad (4)$$

where Φ is the geopotential, ψ is the nondivergent streamfunction, ϕ is the latitude, λ is the longitude, a is the radius of the earth, p is the pressure, $\kappa = R/c_p$, and π is the Exner function $\left[c_p \left(\frac{p}{p_0} \right)^\kappa \right]$, which serves as the vertical coordinate (DE). Equation (3), the nonlinear balance condition of Charney (1955), relates the wind and pressure fields according to the assumption that the rotational part of the flow is much larger than the divergent part of the flow, which has been shown to be a good approximation to observed atmospheric flows, especially for

375 flows of the synoptic scale (e.g., Davis et al. 1996). The unbalanced portion of the flow
376 corresponds primarily to the nondivergent component of the ageostrophic wind and cannot be
377 recovered using PV inversion techniques (Davis et al. 1996). The nondivergent flow field
378 recovered from piecewise PV inversion was compared to the pure ERA5 flow field across a
379 $10^\circ \times 10^\circ$ box centered on the NV19 MSLP minimum. Differences between these two flow
380 fields did not exceed 20% for 950 hPa, 10% for 900 hPa, and 5% at and above 850 hPa
381 meaning that piecewise PV inversion is accurately representing this development throughout
382 the troposphere. These larger differences near the surface are directly attributed to stronger
383 nondivergent ageostrophic components of the wind in the vicinity of the intense NV19
384 cyclone.

385 Piecewise PV inversion is accomplished by first performing an inversion on the full
386 perturbation PV which is defined by subtracting the 2-month mean PV from the instantaneous
387 PV at 1-hour increments at each grid point during the development of the NV19 storm. For
388 the full perturbation PV inversion, equations (3) and (4) are solved simultaneously for the
389 hourly Φ and ψ , with the lateral boundary conditions for Φ and ψ prescribed by subtracting
390 the 2-month mean Φ and ψ from the instantaneous ERA5 data. The boundary ψ was
391 initialized using Neumann boundary conditions such that the component of the total wind
392 from the ERA5 data which was perpendicular to the boundary was equivalent to the gradient
393 of ψ along that same boundary, and that the net divergence out of the domain was zero.
394 Neumann boundary conditions consistent with hydrostatic balance were prescribed along the
395 bottom (top) of the domain such that the vertically-averaged perturbation potential
396 temperature, defined following the same method used in calculating the perturbation PV,
397 between 1000 hPa and 950 hPa (150 hPa and 100 hPa) were used to define Φ and ψ along the
398 bottom (top) of the domain. Full static PV inversion was performed across the entire
399 horizontal and vertical domain and, in order to assure a stable solution of equations (3) and
400 (4), negative PV values were manually adjusted to a small positive constant of 0.01 PVU

401 (where $1 \text{ PVU} = 10^{-6} \text{ K m}^2 \text{ kg}^{-1} \text{ s}^{-1}$) and the static stability was required to remain positive
402 throughout the domain. The threshold for convergence was set to 0.1 meter, the over-
403 relaxation parameters for Φ and ψ were 1.8 and 1.9, respectively, and the under-relaxation
404 parameter was set to 0.3. Each hourly time-step reached convergence after approximately 150
405 iterations. The reader is referred to DE for a complete description of the boundary conditions
406 and numerical methods used to solve this system.

407 *c. Partitioning method*

408 The next step in performing piecewise PV inversion is to partition the full
409 perturbation PV field into three distinct pieces. Here we follow a modified version of the
410 piecewise partitioning described in Davis (1992), Korner and Martin (2000), and Winters and
411 Martin (2017) and use relative humidity criteria. Tests were conducted to ensure results were
412 not significantly dependent on the choice of relative humidity threshold (not shown).

413 The three-way partitioning method used in this study is depicted in Figure 8. The
414 surface PV (SFC) is defined as perturbation PV between 950 hPa and 700 hPa in air with a
415 relative humidity $< 95\%$, and also includes the perturbation potential temperature on the
416 bottom boundary of the domain. SFC is designed to represent the influence of near-surface
417 potential temperature perturbations on the flow throughout the domain, as these are equivalent
418 to PV perturbations along the bottom boundary (Bretherton 1966). The interior PV (INT) is
419 defined as the perturbation PV between 950 hPa and 150 hPa found in air with a relative
420 humidity $\geq 95\%$. INT is designed to represent the influence of diabatic generation and
421 erosion of PV associated with latent heat release, a process central to DRW propagation
422 (Boettcher and Wernli 2013). The upper-tropospheric PV (UPTROP) is defined as the
423 perturbation PV between 650 hPa and 150 hPa found in air with a relative humidity $< 95\%$
424 and includes the perturbation potential temperature on the top boundary of the domain.
425 UPTROP is designed to isolate the role of dry middle- and upper-tropospheric, and

426 stratospheric PV intrusions on the flow, along with stratospheric potential temperature
427 anomalies.

428 Static inversion is performed for the SFC and UPTROP PV as for the full
429 perturbation PV, but with Φ and ψ on the horizontal boundaries being set to zero. Inversion
430 of the INT PV is not performed; rather, its associated Φ and ψ (Φ_{INT} and ψ_{INT} , respectively)
431 are presented as:

$$\Phi_{INT} = \Phi_{FULL\ PERT} - (\Phi_{SFC} + \Phi_{UPTROP}) \quad (5)$$

432 and

$$\psi_{INT} = \psi_{FULL\ PERT} - (\psi_{SFC} + \psi_{UPTROP}) \quad (6)$$

433 where Φ_{INT} and ψ_{INT} on the horizontal boundaries are set equal to the full perturbation Φ and
434 ψ , not zero. The decision to prescribe these results was motivated by numerous trials and
435 errors in which the static inversion of the INT PV, though reaching convergence, consistently
436 returned unphysical results. Similar unphysical results are detailed in both Ahmadi-Givi et al.
437 (2004) and Bracegirdle and Gray (2009). Those studies concluded that such results derive
438 from a breakdown of the Charney nonlinear balance condition (Charney 1955) in regions
439 where strong divergence becomes collocated with regions of strong diabatic heating. The
440 development of the NV19 DRW was strongly influenced by diabatic heating collocated with
441 the lower-tropospheric vortex, hence, the governing physics were well outside the requisite
442 nonlinear balance in equation (3). In such situations, convergence to a solution for the INT
443 PV, characterized by heavy diabatic modification for extended periods of time, will produce a
444 result in which the wind field is not dynamically consistent with the pressure field and the DE
445 system of equations for piecewise PV inversion will no longer be valid. As the present
446 analysis seeks to isolate the influence of the INT PV on aspects of the development,
447 calculating it as a residual affords a tenable means to that end given the circumstances. This

448 residual also predominantly corresponds to diabatic processes, as the influences of radiation
449 and turbulence on the PV are much smaller in magnitude on the timescales considered.

450 **4. Results**

451 Subsequent analysis will concentrate on the 950 hPa isobaric surface as this level was the
452 lowest available isobaric surface in the inversion output. Figure 9 compares 950 hPa
453 geopotential height (ϕ_{950}) at the location of the 950 hPa vorticity maximum of the NV19
454 storm from the ERA5 analyses and the full perturbation PV inversion. Though the full
455 inversion results consistently return a higher ϕ_{950} , the hourly positions demonstrate excellent
456 agreement. As the analysis is primarily concerned with the perturbation PV introduced into
457 the domain by the NV19 storm, results of inverting the 2-month mean PV are not discussed.

458 *a. Piecewise frontogenesis*

459 Piecewise PV inversion allows computation of the horizontal frontogenesis function using
460 the recovered balanced flow from the inversion of the full column perturbation PV and each
461 of the three partitioned pieces of the perturbation PV. The goal is to determine which features
462 in the perturbation PV distribution are controlling the strength and evolution of lower-
463 tropospheric frontogenesis (e.g. Ramos 1997). The focus is put on the early cyclogenesis
464 phase as strong lower-tropospheric frontogenesis, its associated ascent, and the resulting
465 intense column stretching were the initial cyclogenetic drivers of the NV19 storm (Figs. 1d,
466 2d).

467 1) 1200 UTC 25 November 2019

468 Ascent during the initial development of the NV19 storm was situated on the warm side
469 of a frontogenesis maximum at 850 hPa forced by differential θ advection by the FULL
470 PERT balanced flow (Fig. 10a). There is good agreement between the distribution and

471 orientation of the frontogenesis calculated using the FULL PERT balanced flow and the
472 frontogenesis calculated using the ERA5 horizontal winds (compare Fig. 1d and Fig. 10a). A
473 majority of the FULL PERT frontogenesis was forced by the UPTROP PV balanced flow
474 associated with the upstream upper-tropospheric shortwave (Fig. 1f and 10b). The balanced
475 flow associated with the INT PV resulted in no notable frontogenesis along the cross section
476 at this time (Fig. 10c). A strong, negative INT PV anomaly in the upper-troposphere was
477 located directly above the development region (not shown) due to persistent, differential
478 lower-tropospheric high θ_e flow fueling convection along the baroclinic zone (e.g. Fig 6a).
479 Despite the emergence of a lower-tropospheric positive INT PV anomaly in response to the
480 associated heating, the negative (upper-tropospheric) piece of the INT PV exerted the
481 predominant influence on the total INT PV-induced flow in the development region and
482 consequently INT PV contributed only negligible frontogenesis. The remaining portion of the
483 lower-tropospheric frontogenesis was forced by the SFC PV balanced flow (Fig. 10d). This
484 portion of perturbation frontogenesis is a result of anomalously warm near-surface potential
485 temperatures underneath the 950 and 850 hPa thermal ridge stretching southwest of the
486 development region which facilitated strong differential warm air advection in the lower-
487 troposphere across the baroclinic zone (Fig. 1a,c).

488 2) 0000 UTC 26 November 2019

489 The FULL PERT frontogenesis function became focused in the lower-troposphere as the
490 DRW vortex developed into a weak center of low pressure (Fig. 10e). There was still good
491 agreement between the frontogenesis calculated using the FULL PERT balanced flow and the
492 frontogenesis calculated using the ERA5 horizontal winds (compare Fig. 2d and Fig. 10e).
493 The perturbation frontogenesis forced by the UPTROP PV balanced flow now occupied a
494 much smaller depth and was weaker as compared to twelve hours prior (Fig. 10b,f). The
495 DRW was still situated beneath an upper-tropospheric negative INT PV anomaly, and so the

496 balanced flow from the INT PV once again resulted in insubstantial perturbation
497 frontogenesis (Fig. 10g). At this time, the majority of the lower-tropospheric frontogenesis
498 appeared forced by the balanced flow attributable to lower-tropospheric potential temperature
499 perturbations (Fig. 2a,c and Fig. 10h).

500 *b. Hourly height changes*

501 The intensification of the NV19 storm is assessed by considering the effects of each of
502 the three pieces of the perturbation PV on near-surface height changes recovered from the
503 piecewise PV inversion process. First, perturbation heights from the ERA5, full, UPTROP,
504 and SFC PV inversions, and the INT PV residual, are recorded at the location of the 950 hPa
505 vorticity maximum associated with the NV19 storm. Then the perturbation height change at
506 time t , associated with the ERA5, full perturbation PV, and each of the three pieces, is the
507 result of subtracting the perturbation heights at time $t + 1hr$ from the perturbation heights at
508 time $t - 1hr$ and dividing by the time interval of 2 hrs. The results of these calculations are
509 shown in Fig. 11, which displays the various height changes from 2100 UTC 25 November to
510 0600 UTC 27 November 2019.

511 Perturbation height changes from the ERA5 data and the inversion of the full perturbation
512 PV were negative at the location of the 950hPa vorticity maximum for a majority of the 33-
513 hour analysis period, with peak negative values occurring between 0900 UTC and 1300 UTC
514 26 November before exhibiting a steady increase until the end of the analysis period (Fig.
515 11a). The ERA5 and the full perturbation PV inversion height changes agree fairly well in
516 terms of magnitude and strength of hourly fluctuations. The 12-hour maximum deepening
517 period spanned from 0600 UTC to 1800 UTC 26 November, with the storm having
518 experienced consecutive MSLP falls greater than 1 hPa hr^{-1} beginning at 0900 UTC 26
519 November until making landfall. The influence of surface potential temperature anomalies on
520 near-surface height changes were initially negative, and then were negligible until the NV19

521 storm lost connection to surface baroclinicity after 1600 UTC 26 November (Fig. 11b).
522 Diabatically-induced PV had the most dominant influence throughout an overwhelming
523 majority of the development (Fig. 11c). Near-surface height changes associated with the INT
524 PV residual were negative beginning at 0000 UTC 26 November until the end of the storm
525 lifecycle, including throughout the entire 12-hour maximum deepening period. In fact, INT
526 PV contributed the most negative height changes during the early and late stages of
527 cyclogenesis. The influence of the upper-tropospheric and stratospheric PV (the UPTROP
528 PV) on near-surface height changes was minimal until 1500 UTC 26 November, by which
529 time the developing upper front had finally encroached upon the NV19 storm, quickly
530 inducing strong negative height changes (Fig. 11d). These height changes were the most
531 negative of any associated with the three pieces of the perturbation PV directly outside of the
532 12-hour maximum deepening period. Interrogations of the various physical mechanisms
533 responsible for this period of development, including potential mutual amplification between
534 the lower-level DRW vortex and the upper-level jet/front system, which initially developed
535 independently of each other, will be explored separately in future work.

536 *c. PV superposition*

537 The influence of specific PV anomalies (i.e., UPTROP, INT, and SFC) on the
538 intensification or degradation of the flow throughout the column is described via the PV
539 superposition principle (Davis and Emanuel 1991; Morgan and Nielsen-Gammon 1998). The
540 anomalous flow associated with, for instance, an UPTROP PV anomaly can interact with the
541 INT PV distribution (at a given isobaric level) in such a way as to amplify the magnitude of
542 the INT PV anomaly via horizontal advection. In a statically stable atmosphere, local
543 increases in EPV translate to increases in cyclonic circulation. Additionally, positive
544 advection of lower boundary potential temperature anomalies by any discrete portion of the
545 balanced flow will induce a similar increase in cyclonic circulation (Bretherton 1966).

546 Therefore, any region experiencing positive advection of perturbation EPV by a balanced
547 flow, which would increase the anomalous EPV at a location, will also experience an increase
548 in the perturbation cyclonic circulation. Any such increase is a manifestation of the PV
549 superposition principle.

550 The hour at which the associated perturbation height changes are most negative for the
551 UPTROP, INT, and SFC PV (indicated by the starred times in Figs. 11b-d) are further
552 investigated to determine if such favorable superposition amongst the various balanced flows
553 attributable to the UPTROP, INT, and SFC PV contributed to an increase in the cyclonic flow
554 throughout the column at these times during the NV19 storm.

555 3) 2100 UTC 25 November 2019

556 The initial near-surface height changes of the NV19 storm, from 2100 UTC to 2300 UTC
557 25 November, were predominantly driven by the influence of lower-boundary PV (Fig. 11b).
558 The most negative of these 950 hPa height changes occurred at 2100 UTC 25 November,
559 which corresponds to the time of initial formation of the SLP minimum in the vicinity of the
560 expansive anticyclone over the northeast Pacific Ocean. Cyclonic PV advections (CPVA) by
561 the balanced flow at three different isobaric levels from the inversion of the UPTROP and
562 SFC PV and the INT PV residual at 2100 UTC 25 November are shown in Fig. 12. The
563 yellow contours on each of the nine panels indicate where there is either appreciable CPVA or
564 positive surface potential temperature advection by the balanced flow from a specified
565 perturbation PV anomaly at the given isobaric level. In the upper troposphere, the balanced
566 flows from the UPTROP and INT resulted in CPVA of upper-tropospheric PV to the north of
567 the NV19 storm (Fig. 12a,b) while upper-tropospheric CPVA from the SFC balanced flow
568 was occurring well to the northwest of the storm (Fig. 12c). No distinct diabatically-induced
569 PV anomaly had formed in the mid-troposphere early in the storm lifecycle, so no notable
570 cyclonic advection of this type of PV was occurring (Figs. 12d-f). Cyclonic advection of

571 lower-boundary PV by the UPTROP and INT balanced flows was not occurring in the
572 vicinity of the NV19 storm (Fig. 12g,h). Only the balanced flow from the SFC was resulting
573 in lower-boundary CPVA immediately over the NV19 storm center (Fig. 12i). Therefore, at
574 this early time in storm development, lower-boundary CPVA was being amplified only by
575 SFC anomalies and no substantial mutual cyclonic amplification of PV anomalies throughout
576 the depth of the troposphere was occurring.

577 4) 1400 UTC 26 November 2019

578 A majority of the subsequent cyclogenesis in terms of 950 hPa height changes was
579 attributable to diabatically-induced PV, which dominated near-surface intensification from
580 0000 UTC to 1600 UTC 26 November (Fig. 11c). Near-surface 1-hourly height changes
581 associated with the diabatically-induced PV were most negative at 1400 UTC 26 November,
582 which was during the last hours of the 12-hour period of most rapid deepening. At that time,
583 the balanced flows from the inversion of the UPTROP and INT residual were responsible for
584 CPVA of upper-tropospheric PV directly over the NV19 storm (Fig. 13a,b) while the
585 balanced flow from the inversion of SFC was inducing CPVA well to the northwest (Fig.
586 13c). By this time, diabatic heating had generated a notable cyclonic mid-tropospheric PV
587 anomaly due east of the surface cyclone. CPVA by the UPTROP and INT balanced flows was
588 occurring to the east-southeast of the storm center (Fig. 13d,e). Advection of this mid-
589 tropospheric PV by the balanced SFC winds also occurred directly northeast of the storm
590 (Fig. 13f). No appreciable advection of lower-boundary potential temperature by the
591 UPTROP winds was occurring at this time (Fig. 13g). The balanced flow attributable to the
592 INT resulted in lower-boundary CPVA to the southeast of the NV19 storm (Fig. 13h) while
593 the SFC winds resulted in lower-boundary CPVA directly over the NV19 storm (Fig. 13i).
594 Mutual cyclonic amplification throughout the column was ongoing at this time as CPVA
595 induced by both UPTROP and INT was occurring in the upper-troposphere (Fig. 13a,b),

596 CPVA induced by UPTROP, INT, and SFC was evident in the mid-troposphere (Figs. 13d-f)
597 and CPVA induced by INT and SFC was ongoing in the lower-troposphere (Fig. 13h,i).

598 5) 2200 UTC 26 November 2019

599 Upper-tropospheric PV anomalies dominated near-surface development directly
600 following the 12-hour most rapid deepening period of the NV19 storm (Fig. 11d). Near-
601 surface 1-hourly height changes from the inversion of the UPTROP peaked at 2200 UTC 26
602 November, which was nearly coincident with the time at which the upper-level jet/front
603 system was most intense (not shown). At this time, the winds associated with UPTROP and
604 INT induced CPVA to the east and south of the NV19 storm, respectively (Fig. 14a,b). There
605 was again no advection of upper-tropospheric PV by the SFC balanced flow near the storm at
606 this time (Fig. 14c). Diabatically-induced PV anomalies in the mid-troposphere were weak at
607 this time, with mid-tropospheric CPVA from each piece of the perturbation flow occurring to
608 the east of the storm center (Figs. 14d-f). Lower-boundary CPVA from the UPTROP and INT
609 balanced flows was situated to the southeast of the NV19 storm center (Fig. 14g,h) with no
610 substantial lower-boundary CPVA arising from the SFC balanced flow (Fig. 14i). Therefore,
611 it appears that mutual cyclonic amplification was primarily occurring in the mid-troposphere
612 (Figs. 14d-f) and upper-troposphere (Figs. 14a,b) late in the development of the cyclone.

613 *d. Summary*

614 The foregoing analysis reveals that the early propagation of the NV19 storm was
615 facilitated by column stretching tied to lower-tropospheric frontogenesis along the pre-
616 existing baroclinic zone that was largely forced by differential temperature advection
617 predominantly associated with the UPTROP balanced flow at 1200 UTC 25 November and
618 then by the SFC balanced flow at 0000 UTC 26 November 2019. Analysis of the near-surface
619 height changes suggests that the diabatically-induced INT PV was the most prominent
620 contributor to near-surface height changes during the intensification of the NV19 storm. The

621 upper-tropospheric/lower-stratospheric UPTROP PV contributed the most to near-surface
622 height changes during the last 12 hours of storm intensification just prior to landfall. The
623 lower-tropospheric SFC PV influenced near-surface height changes only very early in the
624 development. The piecewise PV inversion presented here reveals the marginal influence of
625 near-surface heat fluxes, indirectly included in the SFC PV through inclusion of lower-
626 boundary potential temperature anomalies, on the amplification of the NV19 storm – a
627 notable difference from previous piecewise PV inversions of DRW explosive cyclogenesis
628 events (Moore et al. 2008; Rivière et al. 2010).

629 It is also suggested that mutual amplification between discrete pieces of perturbation PV
630 progressed from the lower to the upper-troposphere as the NV19 storm experienced a 29-hour
631 period of uninterrupted 950 hPa height falls. This progression is visualized in schematic form
632 in Fig. 15 with the colored columns representing each piece of the perturbation PV and
633 similarly colored arrows indicating the strength and at which isobaric levels that piece of the
634 perturbation PV contributed to mutual amplification.

635 Early in the lifecycle, only the balanced flow from the INT PV contributed to
636 amplification of another PV anomaly, namely the UPTROP PV (Fig. 15a)- that is, *mutual*
637 amplification was relatively absent. As the storm began its period of rapid intensification,
638 *mutual* amplification became more pervasive as the balanced flow associated with the
639 UPTROP PV amplified the INT anomaly, the balanced flow associated with the INT PV
640 amplified both the UPTROP and SFC anomalies, and the balanced flow associated with the
641 SFC PV served to amplify the INT anomaly (Fig. 15b). The mutual amplification signal at
642 this time was strongest from the SFC PV. Towards the end of the rapid deepening period, the
643 balanced flow associated with the SFC PV continued to amplify the INT anomaly, but the
644 predominant mutual amplification involved the INT and UPTROP PV acting throughout the
645 column (Fig. 15c). At this later time the mutual amplification signal was strongest in
646 association with the mid- to upper-tropospheric PV anomalies. The strength of the INT PV

647 mutual amplification escalated as the NV19 storm matured and the influence of the UPTROP
648 PV mutual amplification progressively extended throughout the whole depth of the
649 troposphere (Fig. 15). The absence of an initial upper-level cyclogenetic precursor, coupled
650 with the upward march of dominant developmental processes, suggests that the NV19 storm
651 underwent a bottom-up development like that of *Lothar* (Wernli et al. 2002).

652 **5. Conclusions and Discussion**

653 Piecewise PV inversion of an extratropical cyclone in late November 2019 reveals a case
654 of explosive DRW development that was predominantly a function of the influence of
655 diabatic generation of PV associated with latent heat release. Only the late stages of
656 cyclogenesis were dominated by upper-tropospheric and lower-stratospheric PV associated
657 with an upper-level jet/front system. Analysis of the piecewise frontogenesis, the 1-hourly
658 height changes at the location of the 950 hPa vorticity maximum, and mutual cyclonic
659 amplification between perturbation PV anomalies in different layers of the troposphere
660 suggest that the NV19 storm followed a bottom-up development similar to that described by
661 Wernli et al. (2002) in association with *Lothar*. The current study is, to the authors'
662 knowledge, unique in that it interrogates the nature of an explosive DRW development over a
663 cold ocean current.

664 Specific findings from the case study include:

- 665 1) The development of the NV19 storm was unusual in several ways; the storm track was
666 notably out of phase with other EC events in the northeast Pacific Ocean, the deepening
667 rate ranked higher than the 90th percentile in two separate climatologies, and the
668 maximum deepening location of this storm occurred further east than any other EC
669 event over the northeast Pacific Ocean in a non-consecutive 30-year period.
- 670 2) Piecewise frontogenesis analysis, or frontogenesis calculated using the balanced flows
671 from the full column perturbation PV and the three partitioned pieces of the

672 perturbation PV, reveals that frontogenesis along the baroclinic zone stretching across
673 the northeast Pacific Ocean was predominantly a function of balanced winds associated
674 with the UPTROP PV as the NV19 storm was first developing and then almost entirely
675 a function of balanced winds associated with the SFC PV as the storm continued to
676 strengthen. Thus, the dominant forcing for the lower-tropospheric frontogenesis that
677 mobilized the DRW was transferred from the upper-troposphere during initial
678 cyclogenesis to the surface layer once more substantial development had begun.

679 3) Height falls associated with lower-tropospheric PV dominated in the very early stages
680 of cyclogenesis via the northward transport of high θ (θ_e) air along the cold front of a
681 cutoff cyclone situated to the west of an expansive anticyclone. There was no signal of
682 mutual cyclonic amplification between perturbation PV anomalies throughout the
683 troposphere during this initial formation as only near-surface amplification of lower-
684 level PV initially occurred.

685 4) Diabatic generation and rearrangement of PV throughout the depth of the troposphere
686 dominated near-surface height falls over the subsequent 16-hour period. These diabatic
687 feedbacks were in response to vigorous lower-tropospheric frontogenesis which was
688 situated along the warm front of the NV19 storm. The diabatic feedbacks conspired to
689 force mutual cyclonic amplification of perturbation PV anomalies notably in the mid-
690 troposphere and extending throughout the depth of the troposphere. This period
691 encompassed the entire 12-hour maximum deepening period during which the storm
692 deepened 34 hPa as it moved southeastward.

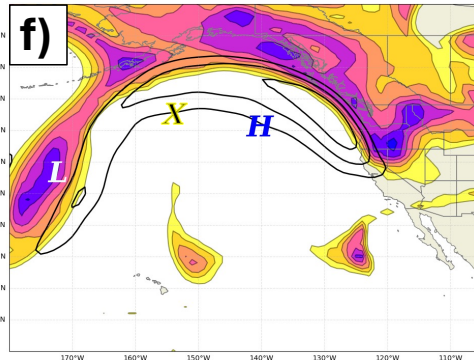
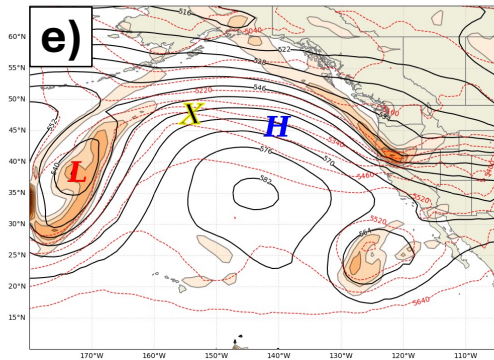
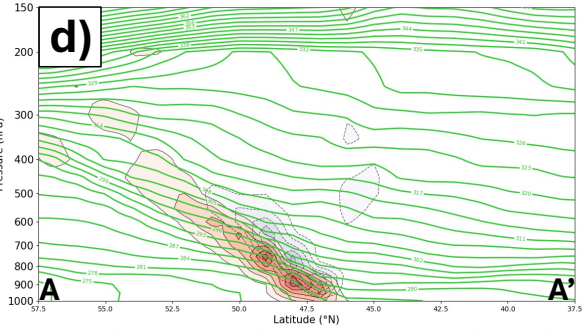
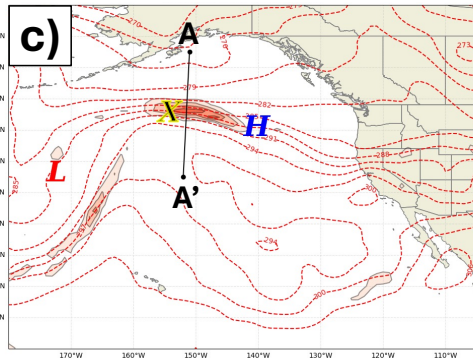
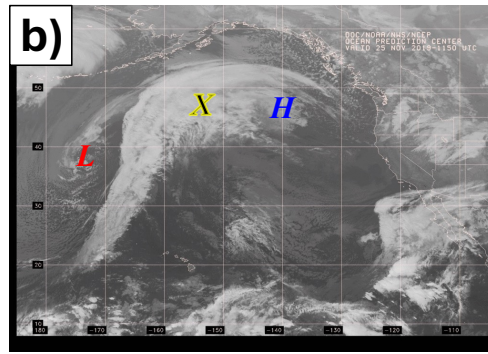
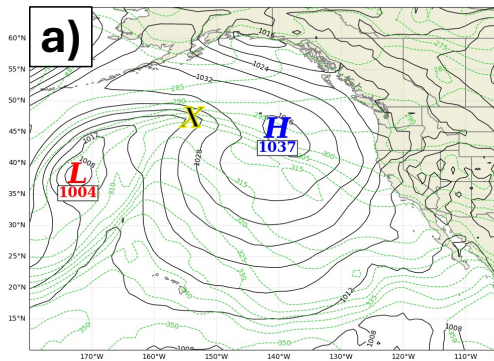
693 5) The final period of development was dominated by upper-tropospheric PV associated
694 with an intense upper-level jet/front system which focused vigorous CVA by the
695 thermal wind directly over the surface cyclone as it approached the coast. Mutual
696 cyclonic amplification was primarily occurring between perturbation PV anomalies in
697 the mid- and upper-troposphere during this final period of deepening.

698 6) The direct effects of near-surface heat fluxes, which are indirectly included in the SFC
699 PV, were quite unimportant to storm intensification in this case of explosive DRW
700 cyclogenesis. In fact, the SFC PV was the *least* important forcing for 950 hPa height
701 falls aside from very early on in the storm lifecycle. This differs from previous
702 piecewise PV inversion studies on rapidly deepening DRWs (Moore et al. 2008;
703 Rivière et al. 2010), which suggests that DRW explosive cyclogenesis occurring over
704 cold ocean currents relies on different circumstances or a different sequencing of
705 forcings for development than DRW explosive cyclogenesis occurring over warm
706 ocean currents.

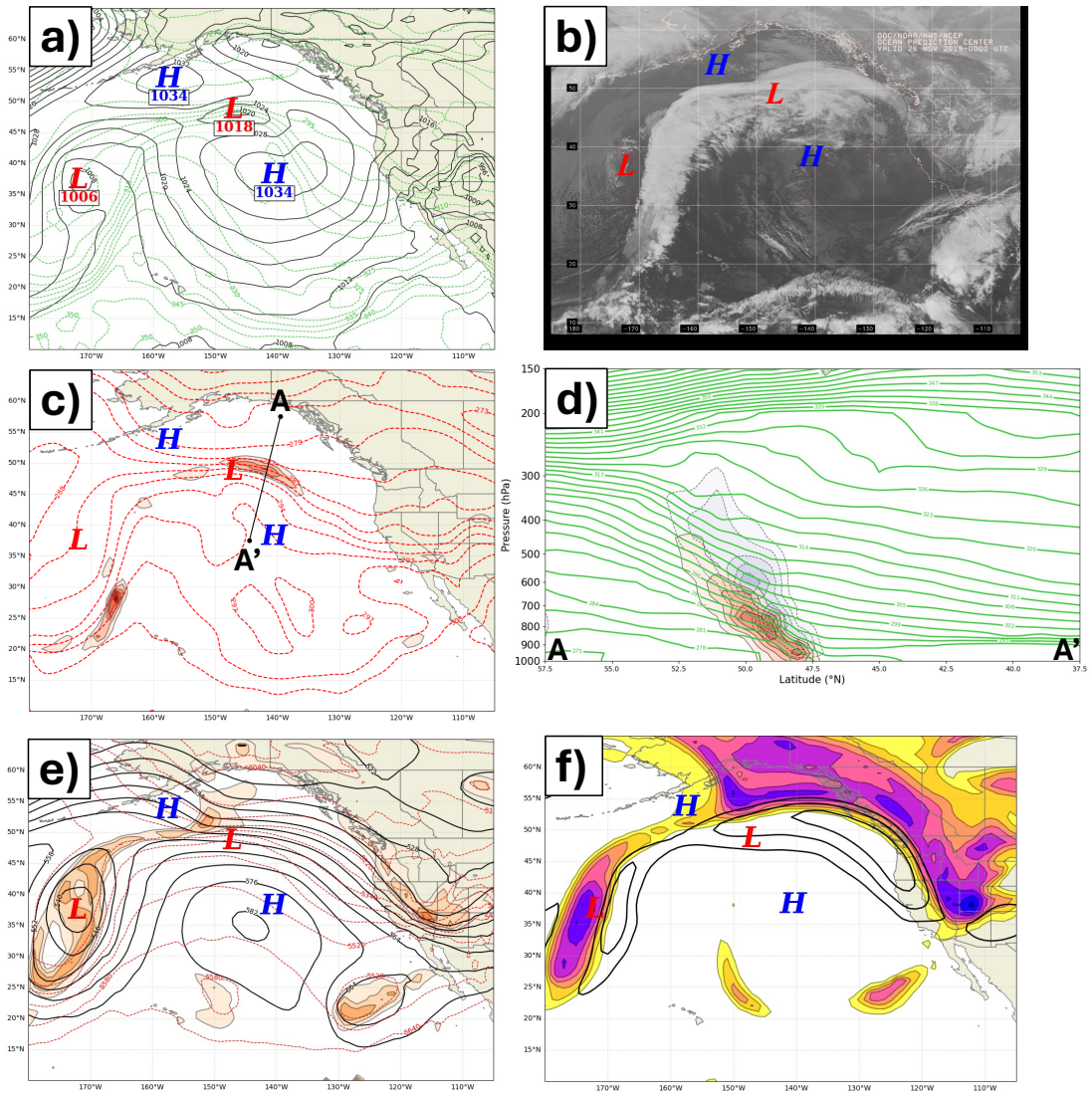
707 Like *Lothar*, the NV19 storm featured a bottom-up rapid intensification of a DRW
708 dependent upon diabatic generation of lower-tropospheric PV to spawn a potent surface
709 cyclone. Despite several similarities, the NV19 storm did not follow the same developmental
710 sequence as *Lothar*. Wernli et al. (2002) showed that the circulation attributable to the lower-
711 tropospheric PV anomaly of *Lothar*, which was produced via intense latent heating, was
712 substantial enough to extend to the jet level and aid in the formation of an upper-tropospheric
713 PV anomaly which then further intensified the low-level PV anomaly through PV
714 superposition (Davis and Emanuel 1991; Morgan and Nielsen-Gammon 1998). Though the
715 preceding analysis does not consider the problem directly, it appears that both the lower- and
716 upper-tropospheric PV anomalies associated with the low-level DRW vortex and upper-level
717 jet/front system, respectively, initially intensified independently of one another. Additionally,
718 it does not appear that the lower-level PV anomaly forced the development of the upper-level
719 PV anomaly, as was the case with *Lothar*.

720 Systematic investigation of whether, and to what degree, the simultaneously
721 strengthening low-level DRW vortex and upper-level jet/front system had notable influences
722 on one another during the NV19 development is a topic for future work. Specific analysis will
723 focus on whether the circulation associated with the low-level DRW vortex contributed to a

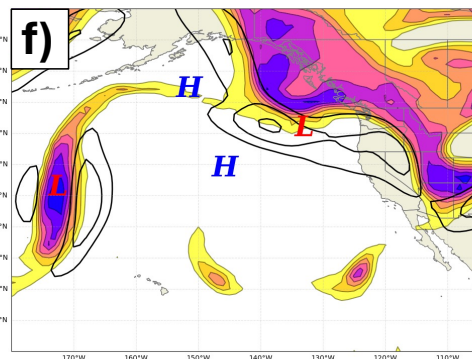
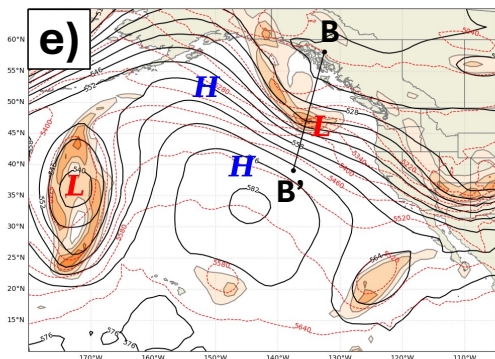
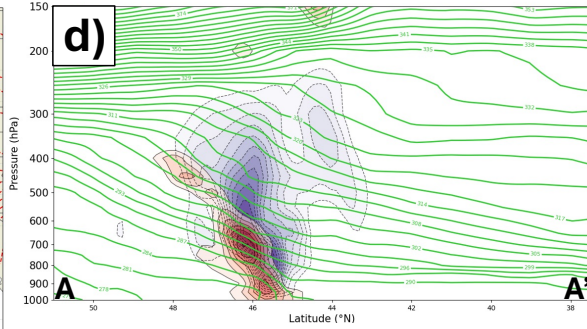
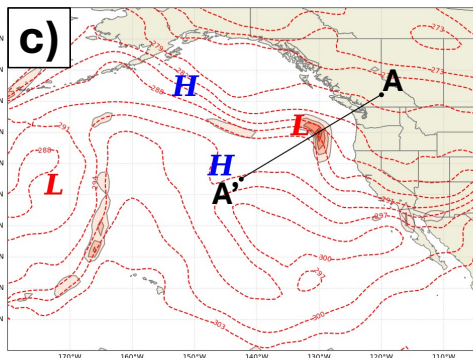
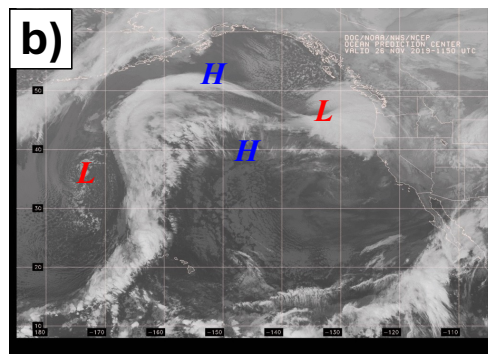
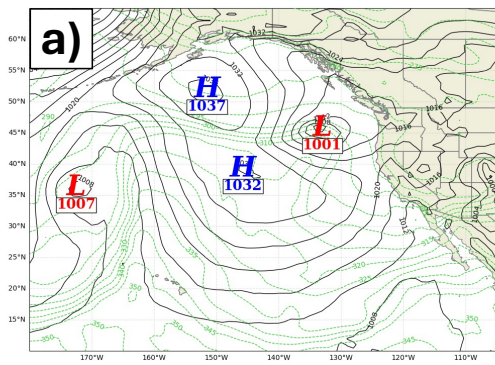
724 mobilization of the “Shapiro effect” (Rotunno et al. 1994) thereby instigating the
725 development of the upper-level jet/front system when the two features superposed. This
726 proposition will be explored using piecewise PV inversion in a forthcoming, complimentary
727 study on this unusual cyclogenesis event.



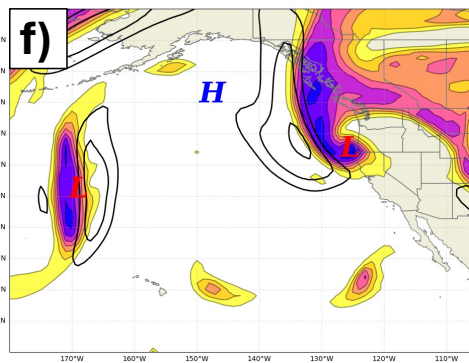
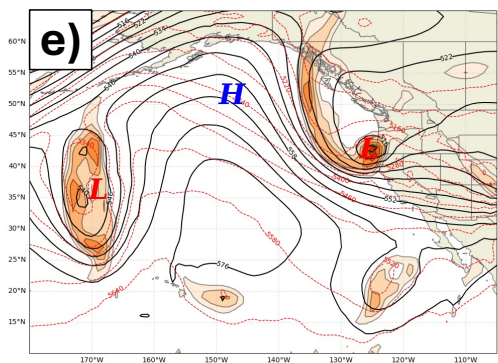
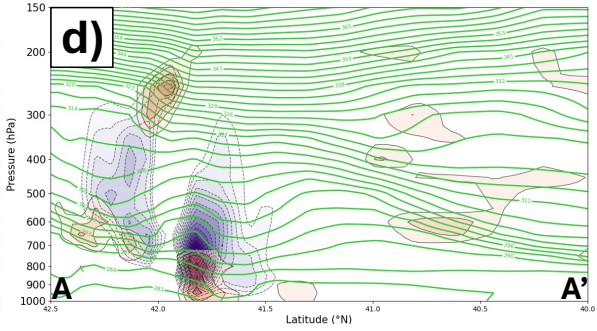
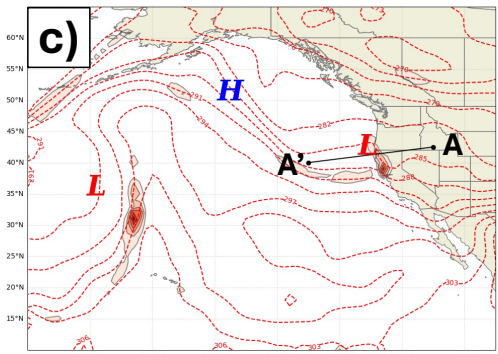
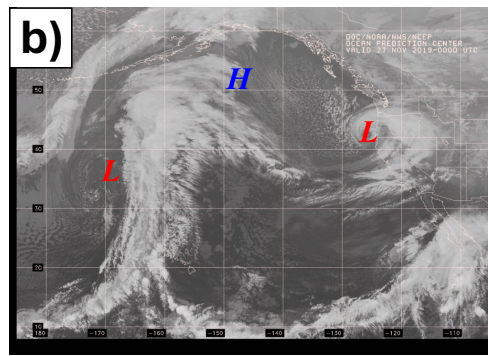
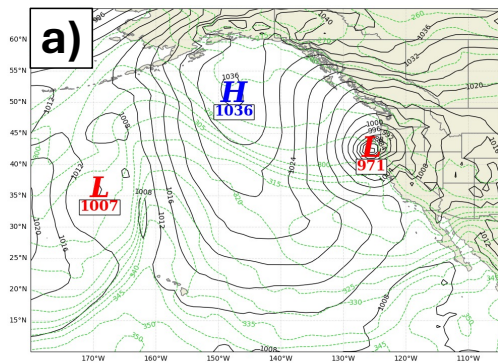
729 Fig. 1. (a) Sea-level pressure and 950 hPa equivalent potential temperature (θ_e) from the
 730 ERA5 reanalysis valid at 1200 UTC 25 November 2019. Solid, black lines are isobars
 731 contoured every 4 hPa. Dashed, green lines are 950 hPa moist isentropes contoured every 5
 732 K. “H” denotes the centers of high pressure systems whereas “L” denotes centers of low
 733 pressure systems. “X” denotes the development region of NV19 storm. (b) GOES-17 infrared
 734 imagery of the northeast Pacific basin valid at 1150 UTC 25 November 2019. “H”, “L”, and
 735 “X” as in panel (a). (c) Potential temperature and positive horizontal frontogenesis at 850 hPa
 736 from the ERA5 reanalysis valid at 1200 UTC 25 November 2019. Dashed, red contours are
 737 isentropes contoured every 3 K. Shading indicates positive frontogenesis function values
 738 shaded every $5 \times 10^{-1} \text{ K (100km)}^{-1} (3\text{hr})^{-1}$ starting at $5 \times 10^{-1} \text{ K (100km)}^{-1} (3\text{hr})^{-1}$. “H”,
 739 “L”, and “X” as in panel (a). Black line indicates the cross section shown in panel (d). (d)
 740 Cross section along A-A’ in panel (c) of potential temperature, frontogenesis, and negative
 741 omega valid at 1200 UTC 25 November 2019. Potential temperature (green) contoured every
 742 3 K starting at 300 K. Positive frontogenesis function (red shading) shaded every $5 \times 10^{-1} \text{ K}$
 743 $(100\text{km})^{-1} (3\text{hr})^{-1}$. Negative omega (purple dashed shading) shaded every $-2 \times 10^{-1} \text{ dPa s}^{-1}$
 744 starting at $-2 \times 10^{-1} \text{ dPa s}^{-1}$. (e) 1000 hPa – 500 hPa thickness and relative vorticity at 500
 745 hPa from the ERA5 reanalysis valid at 1200 UTC 25 November 2019. Red dashed contours
 746 are lines of constant thickness contoured every 60 meters. Shading indicates positive relative
 747 vorticity shaded every $5 \times 10^{-5} \text{ s}^{-1}$ starting at $5 \times 10^{-5} \text{ s}^{-1}$. “H”, “L”, and “X” as in panel
 748 (a). (f) Potential vorticity and wind speed at 300 hPa from the ERA5 reanalysis valid at 1200
 749 UTC 25 November 2019. Solid, black contours are wind speeds contoured every 10 m s^{-1}
 750 starting at 50 m s^{-1} . Shading indicates potential vorticity at 300 hPa shaded every 5×10^{-1}
 751 PVU ($1 \text{ PVU} = 1 \times 10^{-6} \text{ m}^2 \text{ s}^{-1} \text{ K kg}^{-1}$) starting at $5 \times 10^{-1} \text{ PVU}$. “H”, “L”, and “X” as in
 752 panel (a). “L” denoting the low pressure system changed to light blue for visibility.



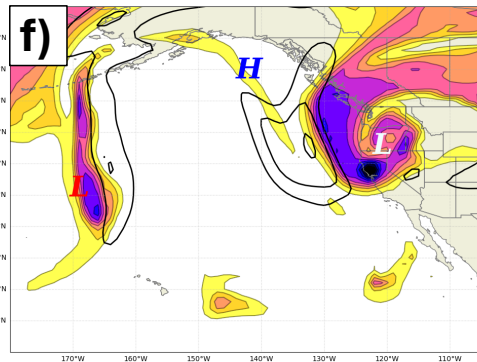
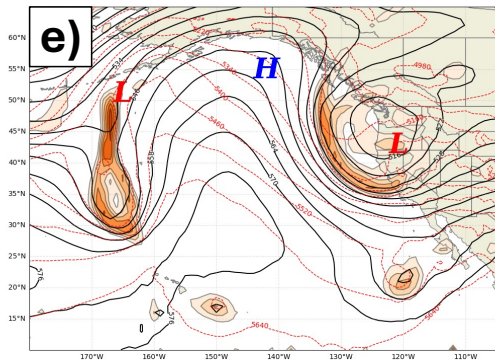
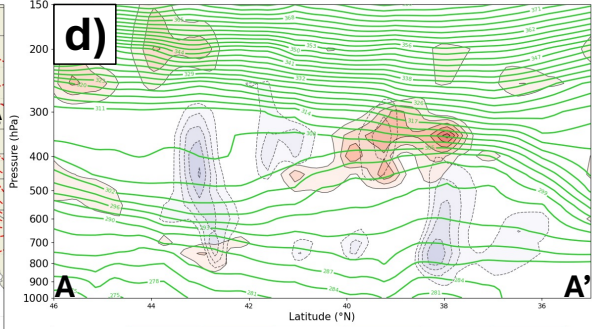
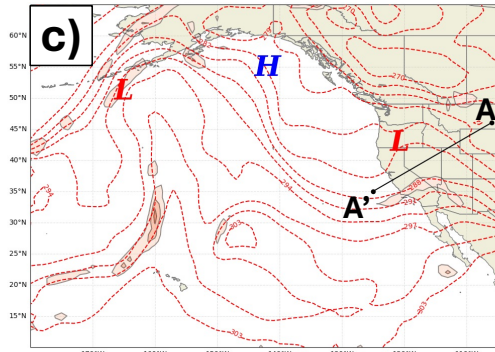
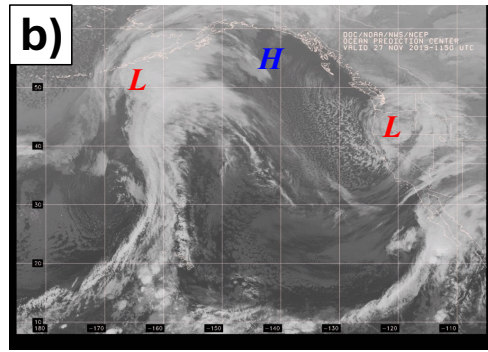
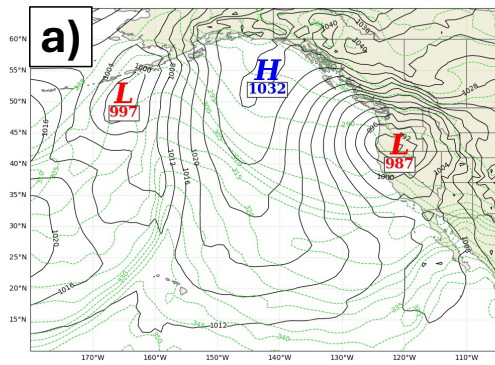
755 Fig. 2. (a) As in Fig. 1a except for 0000 UTC 26 November 2019. (b) As in Fig. 1b except for
756 0000 UTC 26 November 2019. (c) As in Fig. 1c except for 0000 UTC 26 November 2019. (d)
757 As in Fig. 1d except for 0000 UTC 26 November 2019. (e) As in Fig. 1e except for 0000
758 UTC 26 November 2019. (f) As in Fig. 1f except for 0000 UTC 26 November 2019.



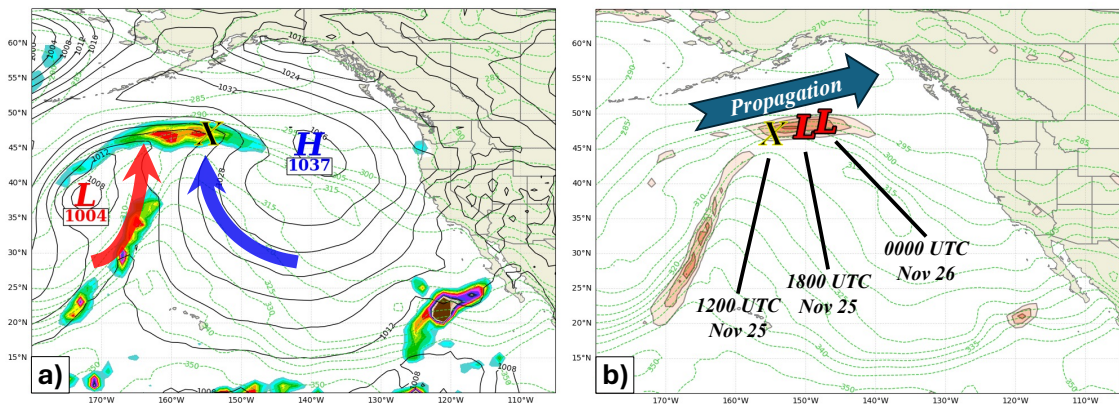
760 Fig. 3. (a) As in Fig. 2a except for 1200 UTC 26 November 2019. (b) As in Fig. 2b except for
761 1150 UTC 26 November 2019. (c) As in Fig. 2c except for 1200 UTC 26 November 2019. (d)
762 As in Fig. 2d except for 1200 UTC 26 November 2019. (e) As in Fig. 2e except for 1200
763 UTC 26 November 2019. (f) As in Fig. 2f except for 1200 UTC 26 November 2019.



765 Fig. 4. (a) As in Fig. 3a except for 0000 UTC 27 November 2019. (b) As in Fig. 3b except for
766 0000 UTC 27 November 2019. (c) As in Fig. 3c except for 0000 UTC 27 November 2019. (d)
767 As in Fig. 3d except for 0000 UTC 27 November 2019. (e) As in Fig. 3e except for 0000
768 UTC 27 November 2019. (f) As in Fig. 3f except for 0000 UTC 27 November 2019.

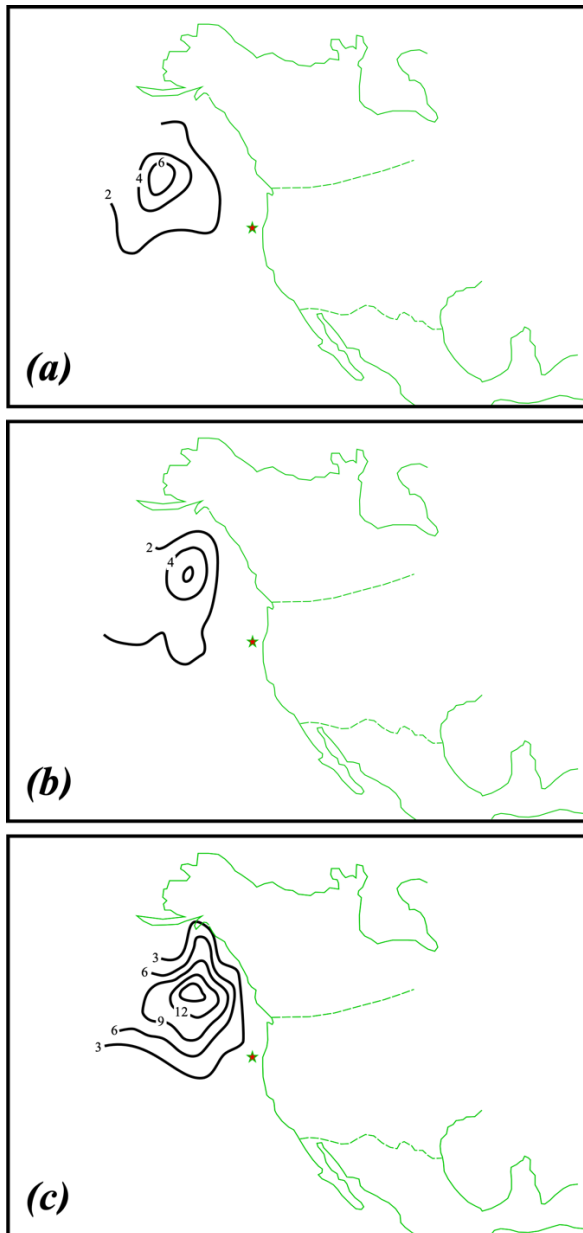


770 Fig. 5. (a) As in Fig. 4a except for 1200 UTC 27 November 2019. (b) As in Fig. 4b except for
771 1150 UTC 27 November 2019. (c) As in Fig. 4c except for 1200 UTC 27 November 2019. (d)
772 As in Fig. 4d except for 1200 UTC 27 November 2019. (e) As in Fig. 4e except for 1200
773 UTC 27 November 2019. (f) As in Fig. 4f except for 1200 UTC 27 November 2019. “L”
774 denoting low pressure system changed to light blue for visibility



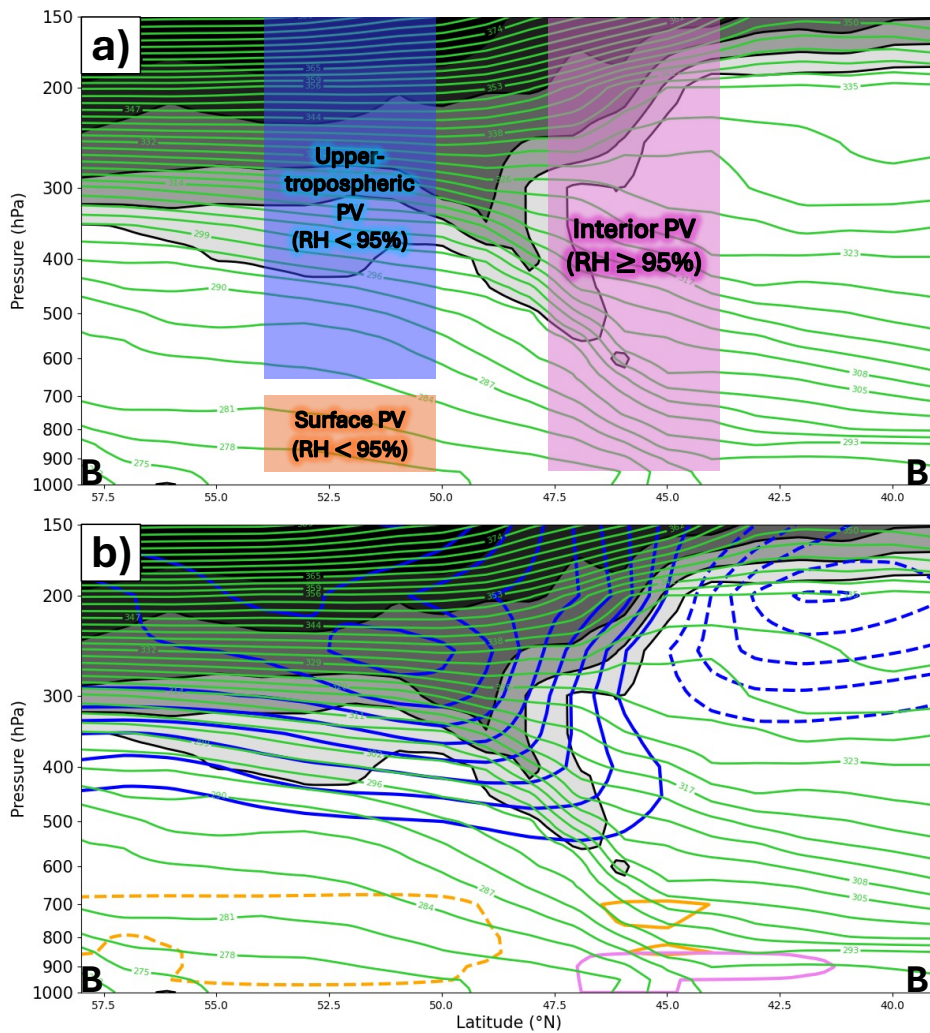
775

776 Fig. 6. (a) Sea-level pressure and 950 hPa equivalent potential temperature (θ_e) from the
 777 ERA5 reanalysis valid at 1200 UTC 25 November 2019. Solid, black lines are isobars
 778 contoured every 4 hPa. Dashed, green lines are 950 hPa moist isentropes contoured every 5
 779 K. Shading indicates the rainfall rate valid at 1800 UTC 25 November 2019 shaded every 1.2
 780 mm 12hr^{-1} starting at $7.2\text{ mm }12\text{hr}^{-1}$. “H” denotes the center of the high pressure system
 781 whereas “L” denotes the centers of the low pressure systems. “X” denotes the development
 782 region of NV19 storm. Red and blue annotated arrows indicate flow induced by the low
 783 pressure system and high pressure system, respectively. (b) Propagation of sea-level pressure
 784 minima along the 12-hour mean 950 hPa θ_e between 1200 UTC 25 November and 0000 UTC
 785 26 November 2019. Shading indicates the 12-hour mean 950 hPa positive horizontal
 786 frontogenesis between 1200 UTC 25 November and 0000 UTC 26 November 2019 shaded
 787 every $0.5\text{ K } (100\text{km})^{-1} (3\text{hr})^{-1}$. Moist isentropes contoured as in (a). “L” and “X” as in panel
 788 (a).



789

790 Fig. 7. Composite of maximum deepening locations (MDL) for “bomb” cyclogenesis events
 791 over the northeastern Pacific Ocean as defined by Sanders and Gyakum (1980) and Zhang et
 792 al. (2017). (a) Adapted from Roebber (1984) for MDL between 1976 and 1982. Red star
 793 indicates MDL for November 2019 storm. (b) Adapted from Wang and Rogers (2001) for
 794 MDL between 1985 and 1996. Red star indicates MDL for November 2019 storm. (c)
 795 Adapted from Zhang et al. (2017) for MDL between 2000 and 2015. Red star indicates MDL
 796 for November 2019 storm.



797

798

Fig. 8. Schematic of the piecewise partitioning scheme used in the inversion of the perturbation PV overlaid on a cross section along B-B' in Fig. 3e. Solid, green contours are

799

potential temperature contoured every 3 K starting at 300 K. Potential vorticity is shaded in

800

gray every 2 PVU (1 PVU = $1 \times 10^{-6} \text{ m}^2 \text{ s}^{-1} \text{ K kg}^{-1}$) starting at 2 PVU. Labeled boxes

801

correspond to the three distinct pieces of the total perturbation PV with the top and bottom

802

boundaries of each box indicating the isobaric layers included within those pieces. Criterion

803

for relative humidity used to distinguish the pieces of PV are as indicated. (b) As in (a), but

804

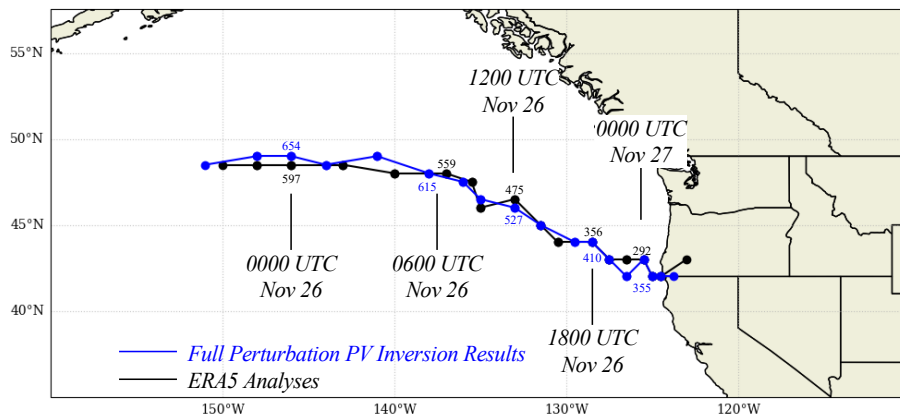
with the distribution of upper-tropospheric perturbation PV (blue contours), interior

805

perturbation PV (pink contours), and surface perturbation PV (orange contours) at 1200 UTC

806

807 26 November 2019 contoured every 0.5 *PVU*. Positive (negative) perturbation PV anomalies
808 denoted by the solid (dashed) contours.



809

810

Fig. 9. Comparison of the full perturbation PV inversion results and the ECMWF

811

reanalysis version 5 (ERA5) analysis of storm track based on location of the 950 hPa vorticity

812

maxima. Location of vorticity maxima in the full perturbation PV inversion results are shown

813

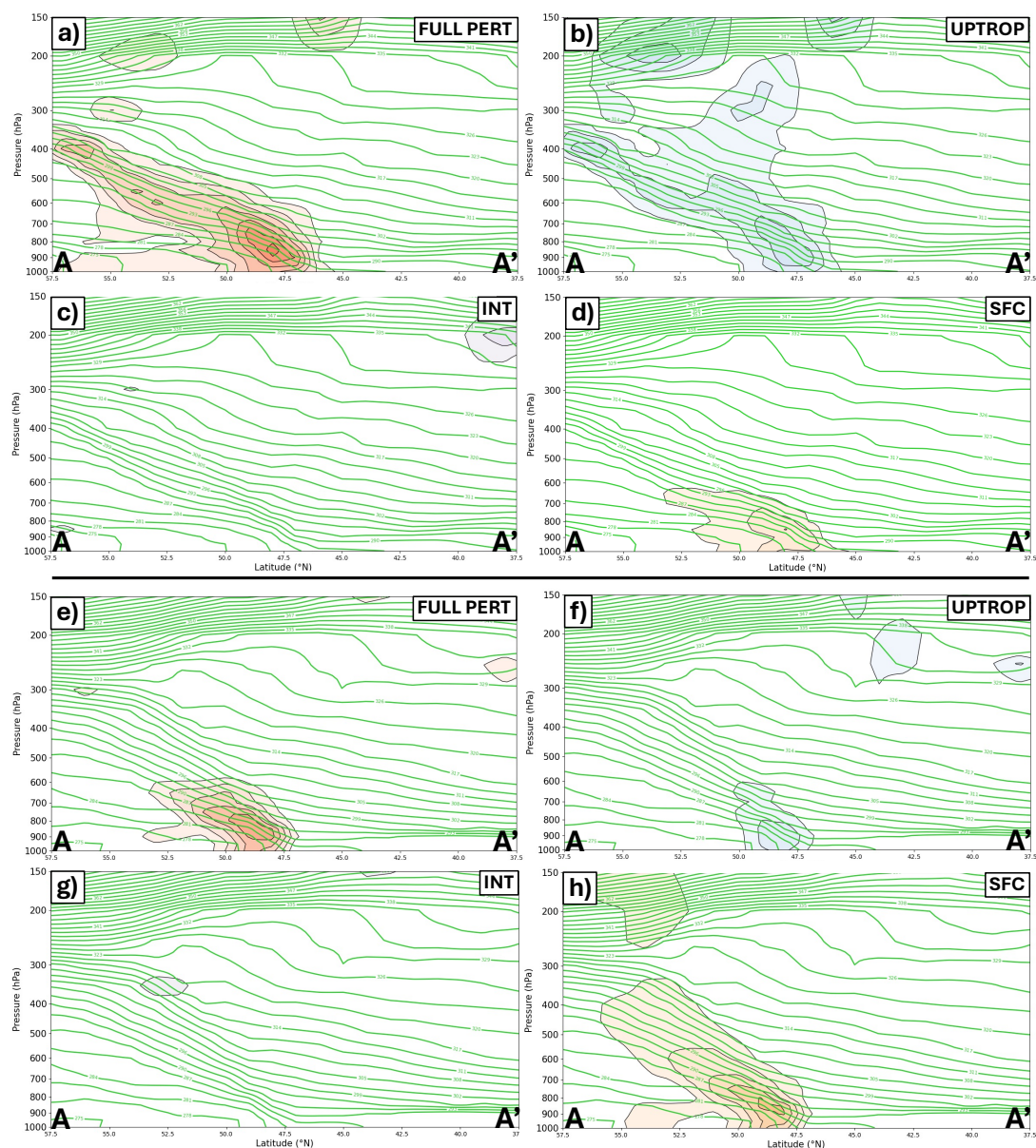
in blue with geopotential height at the vorticity maxima plotted in meters. Location of ERA5

814

analysis vorticity maxima are shown in black with geopotential height at the vorticity maxima

815

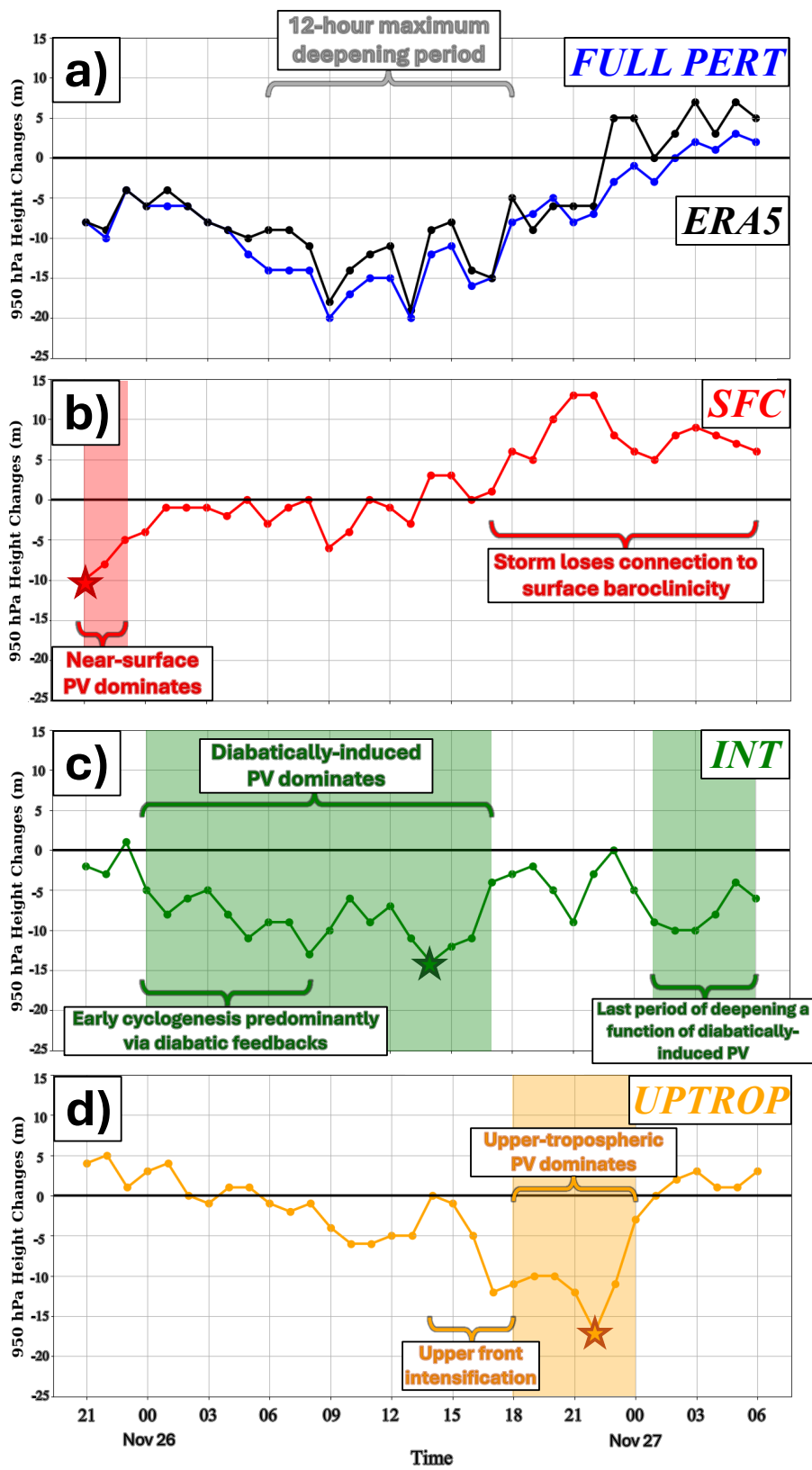
plotted in meters.



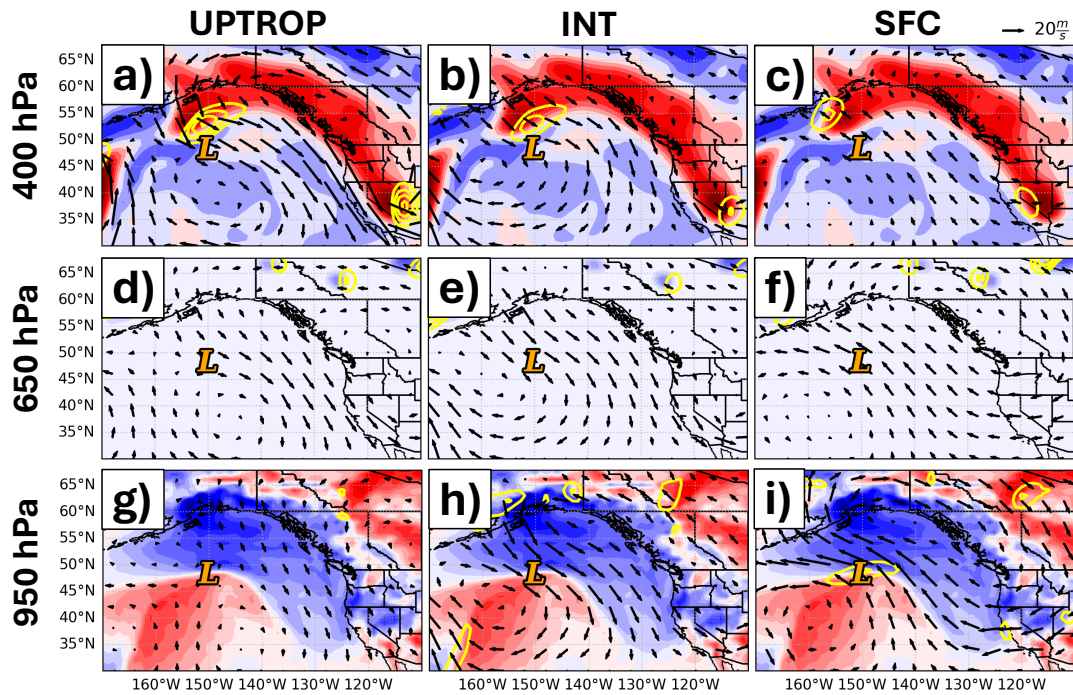
816

817 Fig. 10. Frontogenesis associated with discrete portions of the balanced flow derived from
 818 piecewise PV inversion. (a) Cross section along A-A' in Fig. 1c of potential temperature,
 819 frontogenesis, and negative omega valid at 1200 UTC 25 November 2019. Potential
 820 temperature (green) contoured every 3 K starting at 300 K. Positive frontogenesis function
 821 from the full perturbation PV (FULL PERT) balanced flow (red shading) shaded every
 822 $1 \times 10^{-1} \text{ K (100km)}^{-1} (3\text{hr})^{-1}$. (b) Cross section along A-A' in Fig. 1c of potential
 823 temperature and frontogenesis valid at 1200 UTC 25 November 2019. Potential temperature

824 (green) contoured every 3 K starting at 300 K. Positive frontogenesis function from the
825 UPTROP PV balanced flow (blue shading) shaded every $1 \times 10^{-1} \text{ K (100km)}^{-1} (3\text{hr})^{-1}$. (c) As
826 in panel (b) but for the positive frontogenesis function from the INT PV balanced flow (pink
827 shading). (d) As in panel (c) but for the positive frontogenesis function from the SFC PV
828 balanced flow (orange shading). (e) As in panel (a) but for a cross section along A-A' in Fig.
829 2c valid at 0000 UTC 26 November 2019. (f) As in panel (b) but for a cross section along A-
830 A' in Fig. 2c valid at 0000 UTC 26 November 2019. (g) As in panel (c) but for a cross section
831 along A-A' in Fig. 2c valid at 0000 UTC 26 November 2019. (h) As in panel (d) but for a
832 cross section along A-A' in Fig. 2c valid at 0000 UTC 26 November 2019.



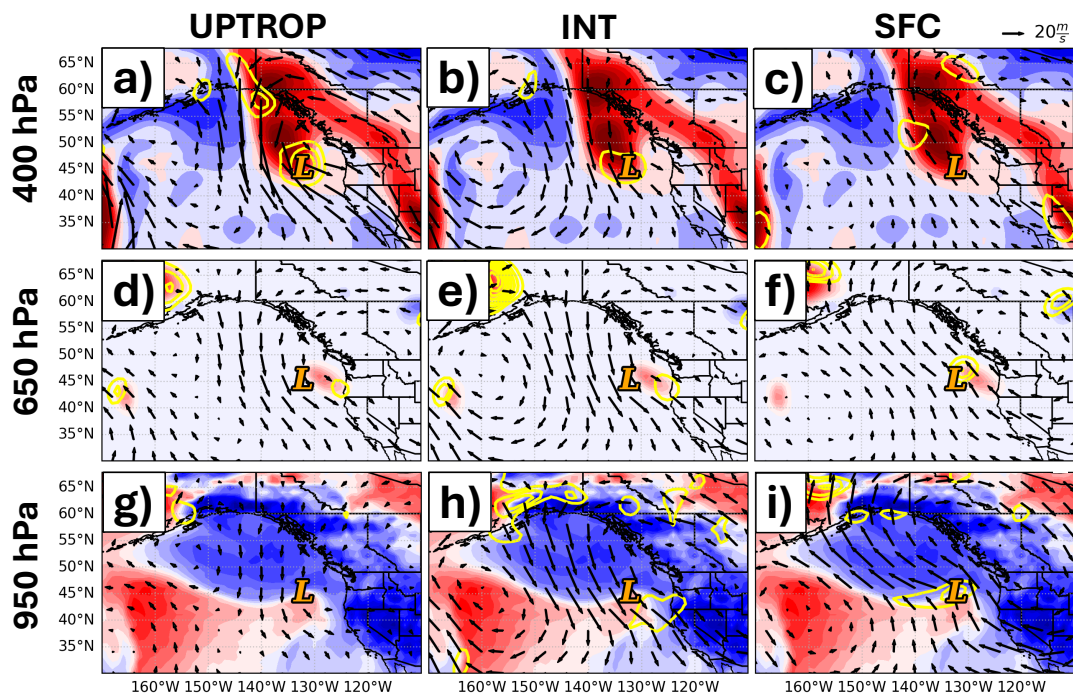
834 Fig. 11. 950 hPa 1-hourly height changes from the inversion of the pieces of the perturbation
835 PV at the location of the 950 hPa vorticity maximum of the November 2019 storm. (a) 950
836 hPa 1-hourly height changes from the inversion of the FULL PERT PV (blue) as defined in
837 Section 3 (see text) along with the observed ERA5 1-hourly height changes (black). Notable
838 time period(s) are annotated. (b) As in (a) but for 1-hourly height changes associated with the
839 SFC PV. Red shading indicates the time period in which the SFC PV contributed the most
840 negative 950 hPa height changes of all three perturbation PV pieces. Red star indicates the
841 time of most negative 950 hPa 1-hourly height change from the SFC PV inversion. (c) As in
842 (b) but for 1-hourly height changes associated with the INT PV. Green shading indicates time
843 periods in which the INT PV contributed the most negative 950 hPa height changes of all
844 three perturbation PV pieces. Green star indicates the time of most negative 950 hPa 1-hourly
845 height change from the INT PV inversion. (d) As in (c) but for 1-hourly height changes
846 associated with the UPTROP PV. Orange shading indicates the time period in which the
847 UPTROP PV contributed the most negative 950 hPa height changes of all three perturbation
848 PV pieces. Orange star indicates the time of most negative 950 hPa 1-hourly height change
849 from the UPTROP PV inversion.



850

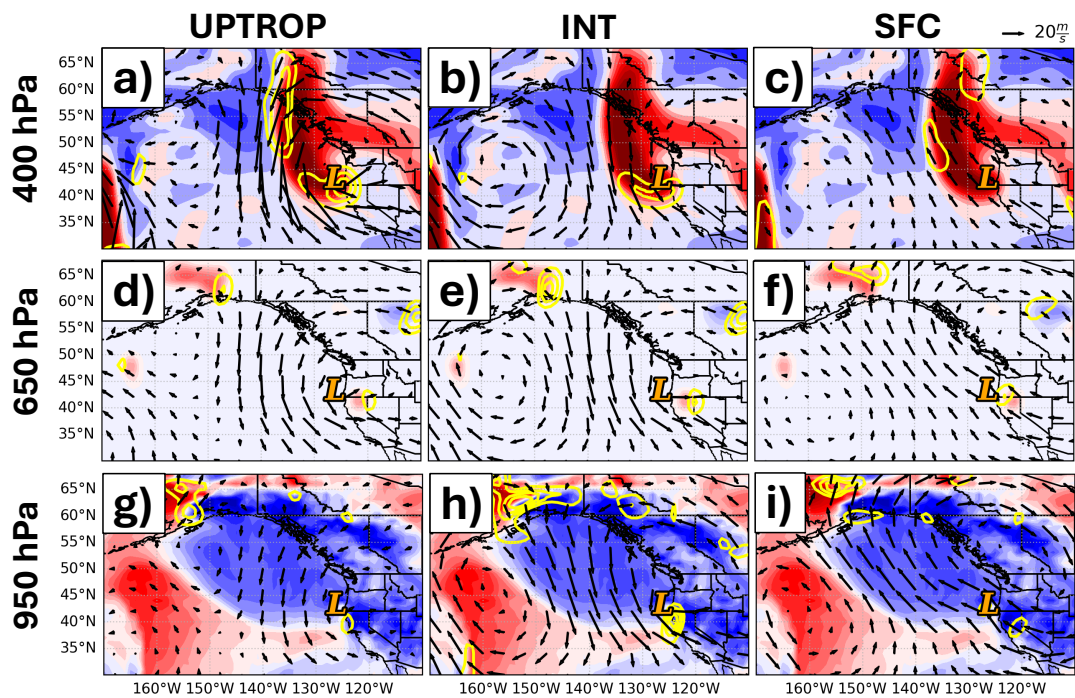
851 Fig. 12. Balanced flow attributable to the UPTROP, INT, and SFC perturbation PV and the
 852 influence of that balanced flow on the 3D PV and potential temperature anomaly structure
 853 valid at 2100 UTC 25 November 2019. (a-c) 400 hPa UPTROP PV anomalies shaded every
 854 5×10^{-1} PVU ($1 \text{ PVU} = 1 \times 10^{-6} \text{ m}^2 \text{ s}^{-1} \text{ K kg}^{-1}$) starting at 5×10^{-1} PVU and 400 hPa
 855 balanced flow (arrows) from the inversion of the (a) UPTROP, (b) INT, and (c) SFC. Yellow,
 856 solid contours represent positive UPTROP PV advection by the (a) UPTROP, (b) INT, and
 857 (c) SFC balanced flows contoured every 1×10^{-1} PVU hr^{-1} starting at 1×10^{-1} PVU hr^{-1} .
 858 Location of the 950 hPa relative vorticity maximum indicated by the orange 'L'. (d-f) 650
 859 hPa INT PV anomalies shaded every 1×10^{-1} PVU starting at 1×10^{-1} PVU and 650 hPa
 860 balanced flow (arrows) from the inversion of the (d) UPTROP, (e) INT, and (f) SFC. Yellow,
 861 solid contours represent positive INT PV advection by the (d) UPTROP, (e) INT, and (f) SFC
 862 balanced flows contoured every starting 1×10^{-2} PVU hr^{-1} at 1×10^{-2} PVU hr^{-1} . Location
 863 of the 950 hPa relative vorticity maximum indicated by the orange 'L'. (g-i) 950 hPa potential
 864 temperature anomalies (SFC PV anomalies) shaded every 1 K and the 950 hPa balanced flow
 865 from the inversion of the (g) UPTROP, (h) INT, and (i) SFC as represented by the arrows.

- 866 Yellow, solid contours represent positive surface potential temperature advection by the (g)
- 867 UPTROP, (h) INT, and (i) SFC balanced flows contoured every 1 K hr^{-1} starting at 1 K hr^{-1} .
- 868 Location of the 950 hPa relative vorticity maximum indicated by the orange 'L'.



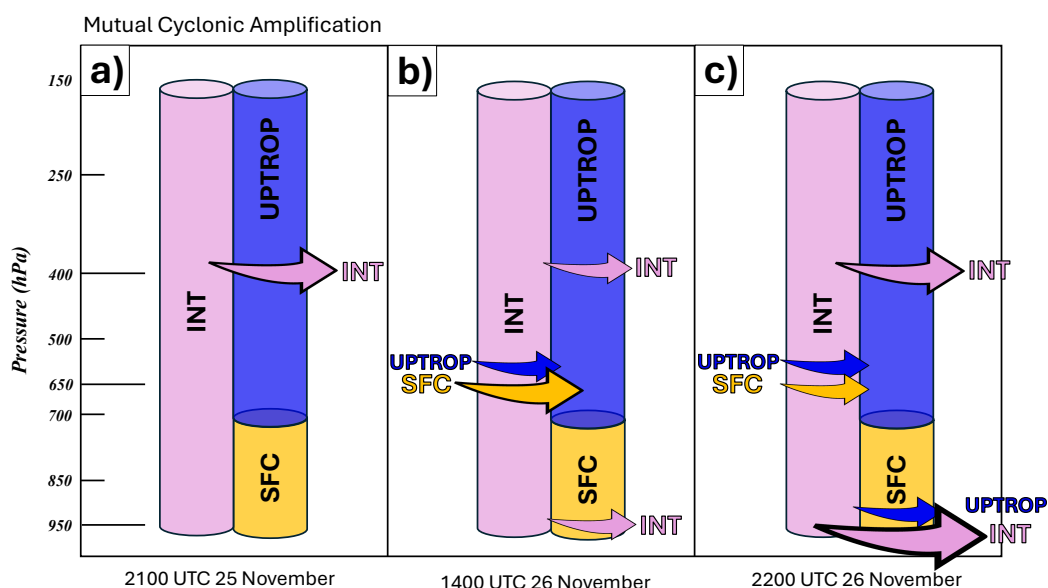
869

870 Fig. 13. (a) As in Fig. 12a except for 1400 UTC 26 November 2019. (b) As in Fig. 12b except
 871 for 1400 UTC 26 November 2019. (c) As in Fig. 12c except for 1400 UTC 26 November
 872 2019. (d) As in Fig. 12d except for 1400 UTC 26 November 2019. (e) As in Fig. 12e except
 873 for 1400 UTC 26 November 2019. (f) As in Fig. 12f except for 1400 UTC 26 November
 874 2019. (g) As in Fig. 12g except for 1400 UTC 26 November 2019. (h) As in Fig. 12h except
 875 for 1400 UTC 26 November 2019. (i) As in Fig. 12i except for 1400 UTC 26 November
 876 2019.



877

878 Fig. 14. (a) As in Fig. 13a except for 2200 UTC 26 November 2019. (b) As in Fig. 13b except
 879 for 2200 UTC 26 November 2019. (c) As in Fig. 13c except for 2200 UTC 26 November
 880 2019. (d) As in Fig. 13d except for 2200 UTC 26 November 2019. (e) As in Fig. 13e except
 881 for 2200 UTC 26 November 2019. (f) As in Fig. 13f except for 2200 UTC 26 November
 882 2019. (g) As in Fig. 13g except for 2200 UTC 26 November 2019. (h) As in Fig. 13h except
 883 for 2200 UTC 26 November 2019. (i) As in Fig. 13i except for 2200 UTC 26 November
 884 2019.



885

886 Fig. 15. Schematic of mutual cyclonic amplification during the development of the November
 887 2019 Northeast Pacific bomb cyclone. Orange, pink, and blue columns represent the positive
 888 perturbation potential vorticity (PV) of the SFC, INT, and UPTROP PV, respectively,
 889 throughout the troposphere and lower stratosphere (see text for definition of SFC, INT, and
 890 UPTROP). Orange, pink, and blue arrows indicate the perturbation balanced flow of the SFC,
 891 INT, and UPTROP PV, respectively, which is resulting in mutual cyclonic amplification at a
 892 specific isobaric level. Size of arrow indicates relative strength of mutual cyclonic
 893 amplification. (a) Mutual cyclonic amplification valid at 2100 UTC 25 November 2019. (b)
 894 Mutual cyclonic amplification valid at 1400 UTC 26 November 2019. (c) Mutual cyclonic
 895 amplification valid at 2200 UTC 26 November 2019.

896 **6. Acknowledgments.**

897 The comments of several reviewers are appreciated and have greatly improved this
898 manuscript. Chris Davis is acknowledged for developing the piecewise PV inversion code
899 used in the analysis. This paper represents a portion of the first author's dissertation at the
900 University of Wisconsin-Madison. The work was supported by the National Science
901 Foundation under Grant AGS-1851152.

902 **7. Data availability statement.**

903 The fifth generation ECMWF atmospheric reanalysis dataset (ERA5) is produced by the
904 Copernicus Climate Change Service (C3S) at ECMWF and can be accessed via
905 <https://cds.climate.copernicus.eu/cdsapp#!/dataset/10.24381/cds.143582cf?tab=overview>.
906 Satellite imagery is produced by the National Centers for Environmental Information at
907 NOAA and can be accessed via <https://www.ncei.noaa.gov/access>. Data used to make in Fig.
908 7 was adapted from Roebber (1984), Wang and Rogers (2001), and Zhang et al. (2017). All
909 computer programs written to perform the data analysis are available from the authors upon
910 request.

911 8. References

- 912 Ahmadi-Givi, F., G. C. Graig, and R. S. Plant, 2004: The dynamics of a midlatitude cyclone with very
913 strong latent-heat release. *Quart J Royal Meteoro Soc*, **130**, 295–323,
914 <https://doi.org/10.1256/qj.02.226>.
- 915 Boettcher, M., and H. Wernli, 2011: Life cycle study of a diabatic Rossby wave as a precursor to
916 rapid cyclogenesis in the North Atlantic—Dynamics and forecast performance. *Monthly*
917 *Weather Review*, **139**, 1861–1878.
- 918 —, and —, 2013: A 10-yr climatology of diabatic Rossby waves in the Northern Hemisphere.
919 *Monthly weather review*, **141**, 1139–1154.
- 920 Bosart, L. F., 1981: The Presidents' Day snowstorm of 18–19 February 1979: A subsynoptic-scale
921 event. *Monthly Weather Review*, **109**, 1542–1566.
- 922 Bracegirdle, T. J., and S. L. Gray, 2009: The dynamics of a polar low assessed using potential
923 vorticity inversion. *Quart J Royal Meteoro Soc*, **135**, 880–893,
924 <https://doi.org/10.1002/qj.411>.
- 925 Bretherton, F. P., 1966: Critical layer instability in baroclinic flows. *Quarterly Journal of the Royal*
926 *Meteorological Society*, **92**, 325–334.
- 927 Charney, J., 1955: The Use of the Primitive Equations of Motion in Numerical Prediction. *Tellus*, **7**,
928 22–26, <https://doi.org/10.1111/j.2153-3490.1955.tb01138.x>.
- 929 Davis, C. A., 1992: Piecewise potential vorticity inversion. *Journal of the atmospheric sciences*, **49**,
930 1397–1411.
- 931 —, and K. A. Emanuel, 1988: Observational evidence for the influence of surface heat fluxes on
932 rapid maritime cyclogenesis. *Monthly Weather Review*, **116**, 2649–2659.
- 933 —, and —, 1991: Potential vorticity diagnostics of cyclogenesis. *Monthly weather review*, **119**,
934 1929–1953.
- 935 Davis, C. A., E. D. Grell, and M. A. Shapiro, 1996: The Balanced Dynamical Nature of a Rapidly
936 Intensifying Oceanic Cyclone. *Mon. Wea. Rev.*, **124**, 3–26, [https://doi.org/10.1175/1520-0493\(1996\)124<0003:TBDNOA>2.0.CO;2](https://doi.org/10.1175/1520-0493(1996)124<0003:TBDNOA>2.0.CO;2).
- 938 Ertel, H., 1942: Ein neuer hydrodynamischer wirbelsatz. *Meteorologische Zeitschrift*, **59**, 271–281.
- 939 Gyakum, J. R., and R. E. Danielson, 2000: Analysis of meteorological precursors to ordinary and
940 explosive cyclogenesis in the western North Pacific. *Monthly Weather Review*, **128**, 851–
941 863.
- 942 —, P. J. Roebber, and T. A. Bullock, 1992: The role of antecedent surface vorticity development
943 as a conditioning process in explosive cyclone intensification. *Monthly weather review*,
944 **120**, 1465–1489.

- 945 Heo, K.-Y., K.-J. Ha, and T. Ha, 2019: Explosive Cyclogenesis around the Korean Peninsula in May
 946 2016 from a potential vorticity perspective: case study and numerical simulations.
 947 *Atmosphere*, **10**, 322.
- 948 Hersbach, H., and Coauthors, 2020: The ERA5 global reanalysis. *Quart J Royal Meteorol Soc*, **146**,
 949 1999–2049, <https://doi.org/10.1002/qj.3803>.
- 950 Hoskins, B. J., M. E. McIntyre, and A. W. Robertson, 1985: On the use and significance of isentropic
 951 potential vorticity maps. *Quarterly Journal of the Royal Meteorological Society*, **111**, 877–
 952 946.
- 953 Iizuka, S., M. Shiota, R. Kawamura, and H. Hatsushika, 2013: Influence of the monsoon variability
 954 and sea surface temperature front on the explosive cyclone activity in the vicinity of Japan
 955 during northern winter. *SOLA*, **9**, 1–4.
- 956 Iwao, K., M. Inatsu, and M. Kimoto, 2012: Recent changes in explosively developing extratropical
 957 cyclones over the winter northwestern Pacific. *Journal of Climate*, **25**, 7282–7296.
- 958 Korner, S. O., and J. E. Martin, 2000: Piecewise frontogenesis from a potential vorticity perspective:
 959 Methodology and a case study. *Monthly Weather Review*, **128**, 1266–1288.
- 960 Kouroutzoglou, J., H. Flocas, M. Hatzaki, K. Keay, I. Simmonds, and A. Mavroudis, 2015: On the
 961 dynamics of a case study of explosive cyclogenesis in the Mediterranean. *Meteorology
 962 and Atmospheric Physics*, **127**, 49–73.
- 963 Kuo, Y.-H., S. Low-Nam, and R. J. Reed, 1991: Effects of surface energy fluxes during the early
 964 development and rapid intensification stages of seven explosive cyclones in the western
 965 Atlantic. *Monthly Weather Review*, **119**, 457–476.
- 966 Lackmann, G. M., D. Keyser, and L. F. Bosart, 1997: A Characteristic Life Cycle of Upper-
 967 Tropospheric Cyclogenetic Precursors during the Experiment on Rapidly Intensifying
 968 Cyclones over the Atlantic (ERICA). *Mon. Wea. Rev.*, **125**, 2729–2758,
 969 [https://doi.org/10.1175/1520-0493\(1997\)125<2729:ACLCOU>2.0.CO;2](https://doi.org/10.1175/1520-0493(1997)125<2729:ACLCOU>2.0.CO;2).
- 970 Lagouvardos, K., V. Kotroni, and E. Defer, 2007: The 21–22 January 2004 explosive cyclogenesis
 971 over the Aegean Sea: Observations and model analysis. *Quarterly Journal of the Royal
 972 Meteorological Society: A journal of the atmospheric sciences, applied meteorology and
 973 physical oceanography*, **133**, 1519–1531.
- 974 Lang, A. A., and J. E. Martin, 2012: The structure and evolution of lower stratospheric frontal zones.
 975 Part 1: Examples in northwesterly and southwesterly flow. *Quarterly Journal of the Royal
 976 Meteorological Society*, **138**, 1350–1365.
- 977 Lim, E.-P., and I. Simmonds, 2002: Explosive cyclone development in the Southern Hemisphere and
 978 a comparison with Northern Hemisphere events. *Monthly Weather Review*, **130**, 2188–
 979 2209.
- 980 Martin, J. E., 2014: Quasi-geostrophic diagnosis of the influence of vorticity advection on the
 981 development of upper level jet-front systems. *Quarterly Journal of the Royal
 982 Meteorological Society*, **140**, 2658–2671.

- 983 —, and J. A. Otkin, 2004: The rapid growth and decay of an extratropical cyclone over the central
984 Pacific Ocean. *Weather and forecasting*, **19**, 358–376.
- 985 McKenzie, M. W., 2014: *An analysis of numerical weather prediction of the diabatic Rossby Vortex*.
986 NAVAL POSTGRADUATE SCHOOL MONTEREY CA,.
- 987 Moore, R. W., and M. T. Montgomery, 2004: Reexamining the dynamics of short-scale, diabatic
988 Rossby waves and their role in midlatitude moist cyclogenesis. *Journal of the atmospheric
989 sciences*, **61**, 754–768.
- 990 —, and —, 2005: Analysis of an idealized, three-dimensional diabatic Rossby vortex: A
991 coherent structure of the moist baroclinic atmosphere. *Journal of the atmospheric
992 sciences*, **62**, 2703–2725.
- 993 —, —, and H. C. Davies, 2008: The integral role of a diabatic Rossby vortex in a heavy snowfall
994 event. *Monthly weather review*, **136**, 1878–1897.
- 995 Morgan, M. C., and J. W. Nielsen-Gammon, 1998: Using tropopause maps to diagnose midlatitude
996 weather systems. *Monthly weather review*, **126**, 2555–2579.
- 997 Odell, L., P. Knippertz, S. Pickering, B. Parkes, and A. Roberts, 2013: The Braer storm revisited.
998 *Weather*, **68**, 105–111.
- 999 Parker, D. J., and A. J. Thorpe, 1995: Conditional convective heating in a baroclinic atmosphere: A
1000 model of convective frontogenesis. *Journal of the atmospheric sciences*, **52**, 1699–1711.
- 1001 R. B. Weldon, 1979: Cloud patterns and the upper air wind field, Part IV. National Weather Service
1002 Satellite training note.
- 1003 Ramos, R. A., 1997: The role of latent heat release on the formation of an upper tropospheric
1004 outflow jet. M.S. thesis, Department of Atmospheric and Oceanic Sciences, University of
1005 Wisconsin-Madison. 149 pp.
- 1006 Raymond, D., and H. Jiang, 1990: A theory for long-lived mesoscale convective systems. *Journal of
1007 Atmospheric Sciences*, **47**, 3067–3077.
- 1008 Reed, R. J., and M. D. Albright, 1986: A case study of explosive cyclogenesis in the eastern Pacific.
1009 *Monthly Weather Review*, **114**, 2297–2319.
- 1010 Rivière, G., P. Arbogast, K. Maynard, and A. Joly, 2010: The essential ingredients leading to the
1011 explosive growth stage of the European wind storm Lothar of Christmas 1999. *Quarterly
1012 Journal of the Royal Meteorological Society: A journal of the atmospheric sciences, applied
1013 meteorology and physical oceanography*, **136**, 638–652.
- 1014 Roebber, P. J., 1984: Statistical analysis and updated climatology of explosive cyclones. *Monthly
1015 Weather Review*, **112**, 1577–1589.
- 1016 —, 1989: The role of surface heat and moisture fluxes associated with large-scale ocean current
1017 meanders in maritime cyclogenesis. *Monthly weather review*, **117**, 1676–1694.

- 1018 —, 1993: A diagnostic case study of self-development as an antecedent conditioning process in
1019 explosive cyclogenesis. *Monthly weather review*, **121**, 976–1006.
- 1020 Rossby, C.-G., 1940: Planetary flow pattern in the atmosphere. *Quart. J. Roy. Meteor. Soc.*, **66**, 68–
1021 87.
- 1022 Rotunno, R., W. C. Skamarock, and C. Snyder, 1994: An analysis of frontogenesis in numerical
1023 simulations of baroclinic waves. *Journal of Atmospheric Sciences*, **51**, 3373–3398.
- 1024 Sanders, F., 1986: Explosive cyclogenesis in the west-central North Atlantic Ocean, 1981–84. Part
1025 I: Composite structure and mean behavior. *Monthly weather review*, **114**, 1781–1794.
- 1026 —, and J. R. Gyakum, 1980: Synoptic-dynamic climatology of the “bomb.” *Monthly Weather
1027 Review*, **108**, 1589–1606.
- 1028 Shapiro, M. A., 1981: Frontogenesis and Geostrophically Forced Secondary Circulations in the
1029 Vicinity of Jet Stream-Frontal Zone Systems. *J. Atmos. Sci.*, **38**, 954–973,
1030 [https://doi.org/10.1175/1520-0469\(1981\)038<0954:FAGFSC>2.0.CO;2](https://doi.org/10.1175/1520-0469(1981)038<0954:FAGFSC>2.0.CO;2).
- 1031 —, 1983: Mesoscale weather systems of the central United States. The national STORM
1032 program: Scientific and technological bases and major objectives. UCAR Rep. *Cooperative
1033 Institute for Research in Environmental Sciences*, **78**.
- 1034 Snyder, C., and R. S. Lindzen, 1991: Quasi-geostrophic wave-CISK in an unbounded baroclinic shear.
1035 *Journal of Atmospheric Sciences*, **48**, 76–86.
- 1036 Sutcliffe, R., 1947: A contribution to the problem of development. *Quarterly Journal of the Royal
1037 Meteorological Society*, **73**, 370–383.
- 1038 Wang, C.-C., and J. C. Rogers, 2001: A composite study of explosive cyclogenesis in different sectors
1039 of the North Atlantic. Part I: Cyclone structure and evolution. *Monthly Weather Review*,
1040 **129**, 1481–1499.
- 1041 Wernli, H., S. Dirren, M. A. Liniger, and M. Zillig, 2002: Dynamical aspects of the life cycle of the
1042 winter storm ‘Lothar’(24–26 December 1999). *Quarterly Journal of the Royal
1043 Meteorological Society: A journal of the atmospheric sciences, applied meteorology and
1044 physical oceanography*, **128**, 405–429.
- 1045 Winters, A. C., and J. E. Martin, 2017: Diagnosis of a North American polar–subtropical jet
1046 superposition employing piecewise potential vorticity inversion. *Monthly Weather
1047 Review*, **145**, 1853–1873.
- 1048 Yoshiike, S., and R. Kawamura, 2009: Influence of wintertime large-scale circulation on the
1049 explosively developing cyclones over the western North Pacific and their downstream
1050 effects. *Journal of Geophysical Research: Atmospheres*, **114**.
- 1051 Zhang, G., and Z. Wang, 2018: North Atlantic extratropical Rossby wave breaking during the warm
1052 season: Wave life cycle and role of diabatic heating. *Monthly Weather Review*, **146**, 695–
1053 712.

1054 Zhang, S., G. Fu, C. Lu, and J. Liu, 2017: Characteristics of explosive cyclones over the Northern
1055 Pacific. *Journal of Applied Meteorology and Climatology*, **56**, 3187–3210.

1056